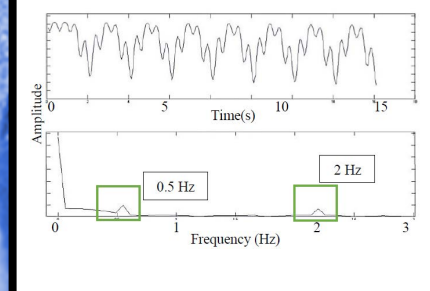
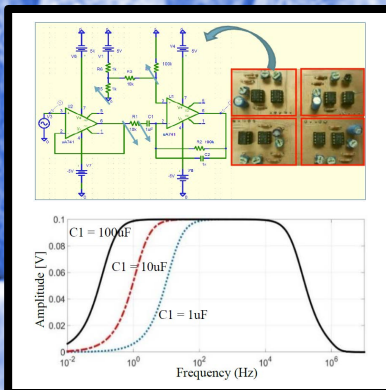
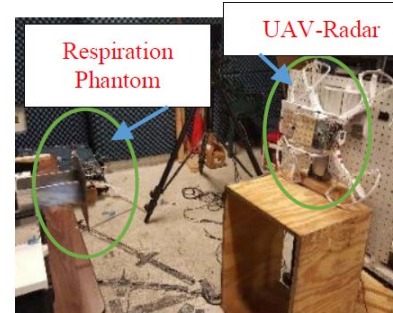


Selected Cover Images
Ashikur Rahman, Yuta Ishii, and Victor Lubecke:
UAV-Radar System for Vital Sign Monitoring
(Bottom Left, Bottom Center, and Right)



APPLIED COMPUTATIONAL ELECTROMAGNETICS SOCIETY EXPRESS JOURNAL

<http://aces-society.org>

GENERAL INFORMATION

PURPOSE AND SCOPE: The Applied Computational Electromagnetics Society (*ACES*) *Express* Journal hereinafter known as the *ACES Express Journal* is devoted to the timely and rapid exchange of information in computational electromagnetics, to the advancement of the state-of-the art, and the promotion of related technical activities. The primary objective of the information exchange is to inform the scientific community in a short amount of time on the developments of recent computational electromagnetics tools and their use in electrical engineering, physics, or related areas. The technical activities promoted by this publication include code validation, performance analysis, and input/output standardization; code or technique optimization and error minimization; innovations in solution technique or in data input/output; identification of new applications for electromagnetics modeling codes and techniques; integration of computational electromagnetics techniques with new computer architectures; and correlation of computational parameters with physical mechanisms.

SUBMISSIONS: The *ACES Express Journal* welcomes original, previously unpublished papers, relating to applied computational electromagnetics. Typical papers will represent the computational electromagnetics aspects of research in electrical engineering, physics, or related disciplines as well as research in the field of applied computational electromagnetics.

Manuscripts are to be submitted through the upload system of *ACES* web site <http://aces-society.org>. Please see "Information for Authors" on inside of back cover and at *ACES* web site. For additional information contact the Editor-in-Chief:

Dr. Ozlem Kilic

Department of Electrical Engineering and Computer Science
The Catholic University of America
Washington, DC 20064
Email: kilic@cua.edu

SUBSCRIPTIONS: All members of the Applied Computational Electromagnetics Society are entitled to access and download the *ACES Express Journal* of any published journal article available at <http://aces-society.org>. *ACES Express Journal* is an online journal and printed copies are not available. Subscription to *ACES* is through the web site.

LIABILITY. Neither *ACES*, nor the *ACES Express Journal* editors, are responsible for any consequence of misinformation or claims, express or implied, in any published material in an *ACES Express Journal* issue. This also applies to advertising, for which only camera-ready copies are accepted. Authors are responsible for all information contained in their papers. If any material submitted for publication includes material which has already been published elsewhere, it is the author's responsibility to obtain written permission to reproduce such material.

THE APPLIED COMPUTATIONAL ELECTROMAGNETICS SOCIETY

<http://aces-society.org>

EDITOR-IN-CHIEF

Ozlem Kilic

Department of Electrical Engineering and Computer Science
The Catholic University of America
Washington, DC 20064

ASSOCIATE EDITORS-IN-CHIEF

Lijun Jiang

University of Hong Kong, Dept. of EEE
Hong, Kong

Steven J. Weiss

US Army Research Laboratory
Adelphi Laboratory Center (RDRL-SER-M)
Adelphi, MD 20783, USA

Amedeo Capozzoli

Universita di Napoli Federico II, DIETI
I-80125 Napoli, Italy

Shinichiro Ohnuki

Nihon University
Tokyo, Japan

William O'Keefe Coburn

US Army Research Laboratory
Adelphi Laboratory Center (RDRL-SER-M)
Adelphi, MD 20783, USA

Yu Mao Wu

Fudan University
Shanghai 200433, China

Kubilay Sertel

The Ohio State University
Columbus, OH 43210, USA

Jiming Song

Iowa State University, ECE Dept.
Ames, IA 50011, USA

Maokun Li

Tsinghua University, EE Dept.
Beijing 100084, China

EDITORIAL ASSISTANTS

Toan K. Vo Dai

The Catholic University of America, EECS Dept.
Washington, DC 20064, USA

Shanell Lopez

Colorado School of Mines, EECS Dept.
Golden, CO 80401, USA

MAY 2016 REVIEWERS

William Coburn

Quang Nguyen

C.J. Reddy

Nghia Tran

Jue Wang

THE APPLIED COMPUTATIONAL ELECTROMAGNETICS SOCIETY EXPRESS JOURNAL

Vol. 1 No. 5

May 2016

TABLE OF CONTENTS

“Effect of Lorentz Force on Motion of Electrolyte in Magnesium Electrolysis Cell” Cheng-Lin Liu, Ze Sun, Gui-Min Lu, Xing-Fu Song, and Jian-Guo Yu	149
“Metamaterial-Inspired Split Ring Monopole Antenna for WLAN Applications” S. Imaculate Rosaline and Singaravelu Raghavan	153
“The Equivalent Circuit Extraction and Application for Arbitrary Shape Graphene Sheet” Ying S. Cao, Li Jun Jiang, and Albert E. Ruehli	157
“A Subwavelength Perfect Absorbing Metamaterial Patch Array Coupled with a Molecular Resonance” Michael F. Finch and Brian A. Lail	161
“Unmanned Aerial Vehicle Platform Stabilization for Remote Radar Life Sensing” Robert H. Nakata, Brian Haruna, Scott K. Clemens, Daren Martin, Charles Jaquiro, and Victor M. Lubecke	165
“Radar Noise Floor Method for Occupancy Detection” Pooja Nuti, Ehsan Yavari, and Olga Boric-Lubecke	169
“UAV-Radar System for Vital Sign Monitoring” Ashikur Rahman, Yuta Ishii, and Victor Lubecke	173

Effect of Lorentz Force on Motion of Electrolyte in Magnesium Electrolysis Cell

Cheng-Lin Liu¹, Ze Sun¹, Gui-Min Lu¹, Xing-Fu Song¹, and Jian-Guo Yu^{1,2}

¹National Engineering Research Center for Integrated Utilization of Salt Lake Resource
East China University of Science and Technology, Shanghai, 200237, China
liuchenglin@ecust.edu.cn, zsun@ecust.edu.cn, gmlu@ecust.edu.cn, xfsong@ecust.edu.cn

²State Key Laboratory of Chemical Engineering
East China University of Science and Technology, Shanghai, 200237, China
jgyu@ecust.edu.cn

Abstract – Magnesium production process is highly energy intensive. Electrolysis process provides an effective route to reduce the energy consumption. In this paper, a three-dimensional electro-magneto-hydrodynamics coupling model of a 120 kA magnesium electrolysis cell using finite element method is presented. In this model, the electric field, magnetic field, and flow field are included. This paper concerns the effects of the Lorentz force on the motion of the electrolyte in the cell. The model predicts that the magnitude of Lorentz force is at its maximum near the region between the anode and cathode. The direction of the Lorentz force is beneficial to the motion of the electrolyte in the magnesium electrolysis cell.

Index Terms – Electro-magneto-hydrodynamics, Lorentz force, magnesium electrolysis cell.

I. INTRODUCTION

Magnesium has found a variety of applications due to a number of advantages including low mass density and high specific strength. Like the Hall-Herault process of aluminum production [1], the electrolysis process for magnesium is one of the most energy intensive industrial processes [2]. Over the years, lots of research efforts have been made on the investigations of the flow field, thermoelectric field, electro-hydrodynamic field, thermoelectromechanical model and magneto-hydrodynamic model by using the commercial software packages [3-7].

Over the years, much attention has been paid on aluminum reduction cell. Little effort, however, has been made on the magnesium electrolysis cell. Shilova and Shcherbinin investigated the distribution of the electromagnetic field with the effects of bus bar and electrode in the magnesium electrolysis cell [8]. The research indicated that the magnetic field will help to improve the circulation and convection of the electrolyte.

Recent years some researches on the multi-physical fields including the electric field, magnetic field and flow fields in magnesium electrolysis cells have been reported [9, 10]. In summary, most of the reported studies of magnesium electrolysis cell only considered the mathematical model based on one physical fields. But little progress has been made on the effect of the Lorentz force on the motion of the electrolyte by using a 3D full cell coupling model of electro-magneto-hydrodynamics fields.

This paper presents an Electro-magneto-hydrodynamics model for the magnesium electrolysis cells to investigate the distributions of electric field, magnetic field and flow field simultaneously. Moreover, the main objective of the article is to show the Lorentz force distribution throughout the cell and its effects on the motion of the electrolyte.

II. DESCRIPTION OF NUMERICAL SIMULATION

A. Structure of magnesium electrolysis cell

In the present article, a 3D full cell model of 120 kA commercial magnesium electrolysis cell with a set top entry of graphite anodes and a set side entry of steel cathodes typically consists of the molten electrolyte of MgCl₂, massive refractory lining, thermal insulating materials, asbestos board, steel shell, capping, and partition wall. The structural parameters used in this work have been reported elsewhere and only a brief description will be given here [11].

B. Governing equations

In the electrolysis process, DC current is fed from the anodes, and flow out from the cathodes after passing through the electrolyte. The study consider the electric field, magnetic field and flow field as the main physical fields in the model. To ensure the feasibility of the model, the following hypotheses are made:

- (a) The model only focuses on the resistance voltage without considering the voltage for the decomposition of magnesium chloride, overvoltage, and contact voltage drop in the cell.
- (b) Anodes are assumed to share all of the current in cells equally.
- (c) All the magnetic line are in the air region.

The problem of electromagnetic analysis is solving Maxwell's equations subject to certain boundary conditions. The Ohm's law is used to predict current distribution as follows:

$$\mathbf{J} = \sigma(\mathbf{E} + \mathbf{v} \times \mathbf{B}). \quad (1)$$

The Lorentz force of the electrolyte is:

$$\mathbf{F} = \mathbf{J} \times \mathbf{B}. \quad (2)$$

Magnetic induction is used for magnetic flux density calculation as follow:

$$\frac{\partial \mathbf{B}}{\partial t} = \nabla \times (\mathbf{v} \times \mathbf{B}) + \frac{1}{\sigma \mu} \nabla^2 \mathbf{B}. \quad (3)$$

$\nabla \times (\mathbf{v} \times \mathbf{B})$ is negligible in comparison with other terms, and reduces to the following:

$$\frac{\partial \mathbf{B}}{\partial t} = \frac{1}{\sigma \mu} \nabla^2 \mathbf{B}. \quad (4)$$

On the supposition that the molecular viscous stress tensor can be neglected in comparison with the turbulent stress tensor, the momentum equation is given as follows:

$$\nabla \times \mathbf{v} = 0, \quad (5)$$

$$\frac{\partial(\rho \mathbf{v})}{\partial t} + (\rho \mathbf{v} \cdot \nabla) \mathbf{v} = -\nabla p + \nu \nabla^2 \mathbf{v} + \rho \mathbf{g} + \mathbf{F}. \quad (6)$$

The k - ε model is used for computing velocity profile of electrolyte using the Lorentz forces (\mathbf{F}) as source term. The k - ε model is a class of turbulent model, called the two-equation model, where the isotropic eddy viscosity is characterized by the turbulent kinetic energy (k) and its dissipation rate (ε), and the equations can be modified to satisfy no-slip boundary conditions at the walls.

B. Boundary conditions

The Neumann boundary condition is adopted at each top of anodes, with the normalized current density of inward current flow equals to the current intensity divided by the working area:

$$-n \cdot \mathbf{J} = J_n. \quad (7)$$

A voltage potential of zero is set at end of cathodes:

$$V = 0. \quad (8)$$

The magnetic vector potential at all of the exterior surfaces of air region is zero:

$$n \times \mathbf{A} = 0. \quad (9)$$

The solutions to these equations are carried out by a finite element software of COMSOL. An optimum number of elements were chosen when two consecutive grid refine elements yield an error less than 1% on both magnetic field and Lorentz force calculations.

III. RESULTS AND DISCUSSION

A. Electromagnetic model validation

It is necessary to validate the accuracy of the mathematical model developed in this article, before using them for numerical experiments. The predicted results are validated by an electromagnetic coil. The coils are shown in Fig. 1 and its structure parameters are shown in Table 1.

Table 1: Technical specifications of the original vice coil of 24009 and 24010

Coil Type	Internal Diameter (mm)	External Diameter (mm)	Length (mm)	Wire Diameter (mm)	Number of Coils
24009	42.9	45.1	66.5	0.22	1150
24010	27.0	29.2	51.7	0.22	370

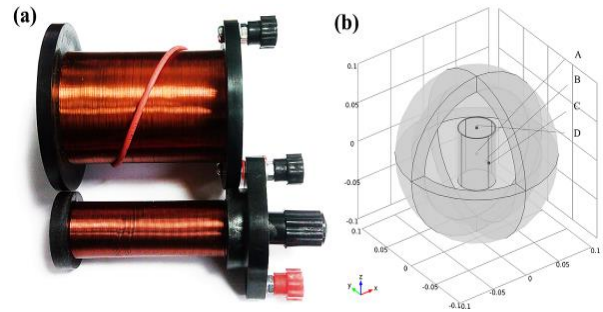


Fig. 1. Electromagnetic coil: (a) experiment, and (b) mathematical model.

The comparison of the magnetic flux density between the experiments and simulations in the position A, B, C, and D of original vice coils are listed in Table 2. Almost all the relative error in the four test points are less than 10%, which shows that the mathematical model can predict the electromagnetic field accurately.

Table 2: Magnetic flux density of experiments and simulations in the different positions of original vice coils

Coil Type	Voltage/V	A/Gs			B/Gs			C/Gs			D/Gs		
		Exp.	Simul.	Relative Error	Exp.	Simul.	Relative Error	Exp.	Simul.	Relative Error	Exp.	Simul.	Relative Error
24009	2.57	47.7	43.6	-8.6%	49.1	43.8	-10.8%	2.5	2.3	-8.0%	9.9	10.8	9.1%
	4.25	77.5	72.2	-6.8%	78.6	72.4	-7.9%	3.5	3.8	8.6%	15.8	17.9	7.8%
	5.92	105.4	100.5	-4.6%	102.6	100.9	-1.7%	5.1	5.3	3.9%	21.9	24.8	8.3%
24010	2.52	70.1	63.2	-9.8%	71.4	63.1	-11.6%	2.1	2	-4.7%	25.2	24.5	-2.8%
	4.19	109.8	104.8	-4.6%	116.2	104.9	-9.7%	3.8	3.4	-10.5%	39.6	40.8	3.0%
	5.84	148.5	146.1	-1.6%	154	146.2	-5.1%	5.3	4.7	-11.3%	54.4	56.9	4.6%

B. Distribution of electromagnetic field

In the magnesium electrolysis cell, current fed from up of the anodes, and flow out from the profile, which form a coil with a quarter of a turn. The magnetic flux density is plotted in Fig. 2. The max of the magnetic flux density is about 270 Gauss (27 mTesla) approximately at the position between the anode and cathode, where is the centre of the “electromagnetic coil”. The magnetic flux density of the magnesium electrolysis cell and aluminum reduction cell are at the same order of magnitude [12].

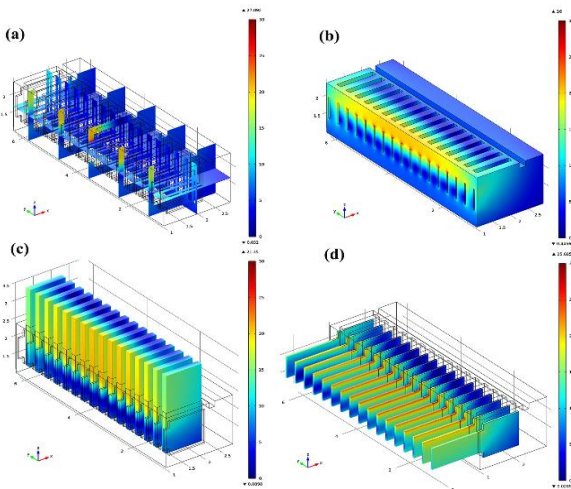


Fig. 2. Magnetic flux density in the magnesium electrolysis cell: (a) slide of electrolyte, (b) electrolyte, (c) anodes, and (d) cathode.

As shown in the Fig. 3, the magnetic flux density in the magnesium electrolysis cell are mainly focused on region between the anode and cathode. The vectors distribution of the magnetic flux density is like a one-fourth of electromagnetic coil.

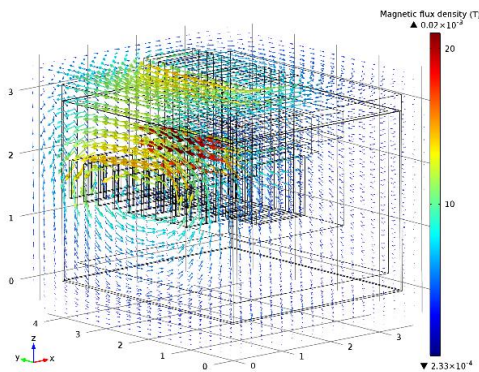


Fig. 3. Vectors of magnetic flux density in the magnesium electrolysis cell.

C. Lorentz force

Lorentz force is an important motive force of the motion of electrolyte in the magnesium electrolysis

processing. In Fig. 4, the typical contour and vector plots of the Lorentz force are plotted in the cell. These results show a high Lorentz force appears between the electrodes in the electrolyte, which is because the higher current density and higher electrolyte velocity. The maximum Lorentz force reaching 93.1 N m^{-3} at corner. And the Lorentz force become lesser toward the collection from electrolysis compartment. This will result in a significant velocity gradient in electrolyte, and may have an influence on the overall flow pattern of the electrolyte in the cell. These results show a high Lorentz force between the electrodes, which is because of the higher current in the region.

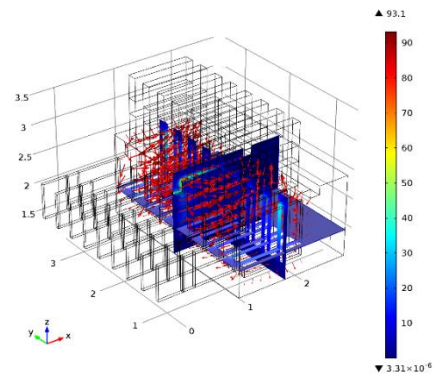


Fig. 4. Lorentz force vectors distribution in the 120 kA magnesium electrolysis cell.

Figure 5 shows the velocity vector and contour plots of the velocity magnitude in the electrolyte of the cell under the effect of the electromagnetic force. The calculated maximum magnitude of the velocity are 0.13 m s^{-1} , at the regions between the electrodes. Velocity decreases toward the center of the cell as the magnetic flux density decreases. The direction of the flow patterns is clearly a function of Lorentz force. Because the Lorentz force is the only volume force in the electrolyte, the motion of the electrolyte in the magnesium electrolysis cell follows the direction of the Lorentz force.

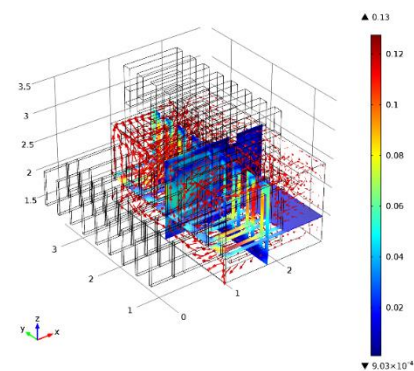


Fig. 5. Velocity vectors distribution in the 120 kA magnesium electrolysis cell.

Figure 6 shows the velocity vector and contour plots of velocity magnitude in the center of the cell ($y = 2.05$ m). The results show a large vortice with clockwise rotation in the cell. It is note that, the directions of Lorentz forces will help improve the circulation of electrolyte and increase the electrolysis efficiency.

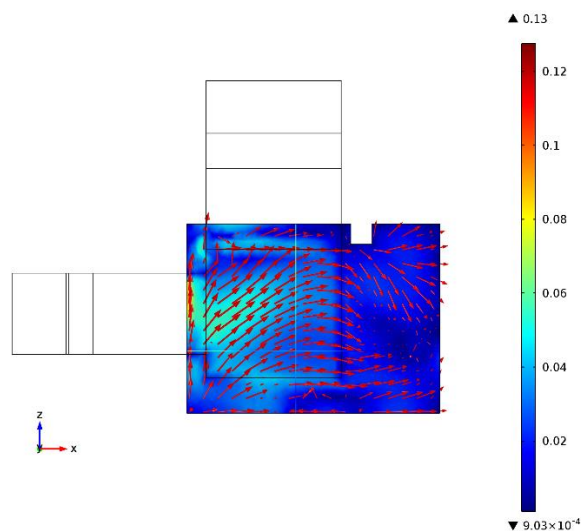


Fig. 6. Velocity vectors and contour plots of velocity magnitude in the center of the cell.

IV. CONCLUSION

A three-dimensional mathematical model of 120 kA magnesium electrolysis cell has been developed using the finite elements method. The electromagnetic field was computed, and its accuracy was validated by an electromagnetic coil. The Lorentz force acting in electrolyte was calculated based on a DC current passing through the cell and the induced magnetic field. On the basis of the electromagnetic field and flow field, the Lorentz force phase was coupled into the electromagnetic field and flow field. The model predicts that the magnitude of Lorentz force is at its maximum near the region between the anode and cathode. The direction of the Lorentz force is beneficial to the motion of the electrolyte in the magnesium electrolysis cell.

ACKNOWLEDGMENT

We acknowledge the financial support provided by National Natural Science Foundation of China (Grant 51504099 and Grant U1407202), and the Fundamental Research Funds for the Central Universities.

REFERENCES

- [1] A. L. Perron, L. I. Kiss, and S. Poncsák, "Mathematical model to evaluate the ohmic resistance caused by the presence of a large number of bubbles in Hall-Héroult cells," *J. Appl. Electrochem.*, vol. 37, pp. 303-310, 2007.
- [2] H. Eklund, P. B. Engseth, B. Langseth, T. Møllerud, and O. Wallevik, *An Improved Process for the Production of Magnesium*. John Wiley & Sons, Inc. 2014.
- [3] K. Zhang, Y. Feng, P. Schwarz, Z. Wang, and M. Cooksey, "Computational fluid dynamics (CFD) modeling of bubble dynamics in the aluminum smelting process," *Ind. Eng. Chem. Res.*, vol. 52, pp. 11378-11390, 2013.
- [4] Z. Zhang, X. Lu, T. Wang, Y. Yan, and S. Chen, "Synthesis and electrolysis of $K_3NaMgCl_6$," *Ind. Eng. Chem. Res.*, vol. 54, pp. 1433-1438, 2015.
- [5] A. Rezvanpour, E. W. C. Lim, and C. Wang, "Computational and experimental studies of electrohydrodynamic atomization for pharmaceutical particle fabrication," *AIChE J.*, vol. 58, pp. 3329-3340, 2012.
- [6] M. Dupuis, "Thermo-electric design of a 740 kA cell, is there a size limit?," *Aluminium: Inter. J. Ind. Res. App.*, vol. 81, pp. 324-327, 2005.
- [7] D. S. Severo, A. F. Schneider, E. C. Pinto, B. Gusberti, and V. Potocnik, "Modeling magneto-hydrodynamics of aluminum electrolysis cells with ANSYS and CFX," *Light Met.*, pp. 475-480, 2005.
- [8] E. I. Shilova and E. V. Shcherbinin, "Control methods MHD convection in the magnesium electrolysis cells," *Magnetohydrodyn.*, vol. 34, pp. 147-152, 1998.
- [9] Z. Sun, H. Zhang, P. Li, B. Li, G. Lu, and J. Yu, "Modeling and simulation of the flow field in the electrolysis of magnesium," *JOM*, vol. 61, pp. 29-33, 2009.
- [10] Z. Sun, Z. Yun, G. Lu, P. Li, J. Wang, and J. Yu, "Novel method based on electric field simulation and optimization for designing an energy-saving magnesium electrolysis cell," *Ind. Eng. Chem. Res.*, vol. 50, pp. 6161-6173, 2011.
- [11] C. Liu, Z. Sun, G. Lu, X. Song, and J. Yu, "Scale-up design of a 300 kA magnesium electrolysis cell based on thermo-electric mathematical models," *Can. J. Chem. Eng.*, vol. 92, pp. 1197-1206, 2014.
- [12] S. Das, G. Brooks, and Y. Morsi, "Theoretical investigation of the inclined sidewall design on magnetohydrodynamic (MHD) forces in an aluminum electrolytic cell," *Metall. Mater. Trans. B.*, vol. 42, pp. 243-253, 2011.

Metamaterial-Inspired Split Ring Monopole Antenna for WLAN Applications

S. Imaculate Rosaline and S. Raghavan

Department of Electronics and Communication Engineering
National Institute of Technology, Tiruchirappalli, India
imaculaterosaline@gmail.com, raghavan@nitt.edu

Abstract — This paper describes the design of a compact dual band monopole antenna for WLAN (2.4/5.2/5.8 GHz) applications. The antenna is printed on a 22.5×24×0.8 mm³ FR-4 substrate with a partial ground plane and is fed by a microstrip line. The proposed structure consists of a simple hexagonal ring with a split arm along its center. The split in the arm in turn creates a quarter wavelength resonance in the higher frequency range. It also induces magnetic resonance which accounts for band notch between the WLAN lower (2.4 GHz) and upper bands (5.2/5.8 GHz). The extraction of negative permeability of the split ring structure is also discussed. A prototype of the proposed structure is fabricated and the measured results comply greatly with the simulated results. The antenna has consistent radiation pattern and stable gain over all the working region.

Index Terms — Hexagonal monopole antenna, negative permeability, notch frequency, split ring, WLAN.

I. INTRODUCTION

Wireless Local Area Network (WLAN) is a significant component of the wireless computer network which interconnects two or more devices. It is based on IEEE 802.11 standard and operates in the 2.45 (2.4-2.48) GHz, 5.2 (5.15-5.35) GHz and 5.8 (5.75-5.825) GHz frequencies. Design of single antenna capable of operating at all these specified frequencies have attracted many researchers in the recent past. Besides obtaining multiple frequencies, the antenna also demands compactness, cost effectiveness and flexibility to be integrated with other microwave integrated devices. Printed monopole antennas seem to be a good choice to meet these aforementioned challenges. Multi branched radiators [1, 2], slotted monopoles [3-5], meander monopoles [6], fractal shapes [7] are few among them to obtain dual band operation in the WLAN 2.5/5.2/5.8 GHz range. However, these antennas suffer from either complicated geometry [1, 5] or larger dimensions. Reactive slots in the radiating patch [3] have compact dimensions, yet it resulted in poor impedance matching at the lower resonant band. Recently, electromagnetic (EM) metamaterials inspired split ring elements and its complementary are also used as

radiating structures for achieving compact and dual band antennas in the WLAN range. Their role in antenna design becomes attractive because of their ability to achieve miniaturization [8, 9], multiband resonances [10] gain and bandwidth enhancement [11]. Split ring monopole antenna proposed in [12] has impedance matching problem in the lower WLAN band, whereas the dual band antennas with CSRRs [13] and triangular split ring resonators (SRRs) [14] has larger dimensions. In general, the overall dimension of these antennas are large compared with the proposed one as shown in Table 1 below. Also, unlike these antenna analysis, this paper emphasizes on the role of metamaterial property (negative permeability) in antenna design, which many papers have failed to prove. As a result, the antenna designer can enjoy the privilege of tuning the operating frequency to the desired range.

In this paper, a simple and compact hexagonal split ring radiating element is proposed for WLAN applications. The split in the ring element is capable of creating band separation (notch band) between the operating bands due to its induced magnetic resonance. The proposed geometry is very simple with good resonant and radiation characteristics, making it a good choice for commercial use.

Table 1: Comparison of the existing antennas with the proposed antenna

Ref.	Dimensions, L x W (mm ²)	Metamaterial Property Verification
[12]	20 x 32	Not verified
[13]	34 x 30	Not verified
[14]	40 x 35	Not verified
Proposed antenna	24 x 22.5	Verified

II. PROPOSED ANTENNA DESIGN

The evolution of the proposed split ring radiating antenna is shown in Fig. 1. Configuration A shows a hexagonal ring monopole fed by a 50 Ω microstrip line and a partial ground plane. The monopole considered in our antenna design is hexagonal in shape whose resonant frequency will be similar to that of a circular monopole

[15], hence the resonant frequency is given as $fr \approx \frac{1.8412 \cdot c}{4\pi S \sqrt{\epsilon_r}}$. Here, c is the velocity of light, S is the side length of the hexagon and ϵ_r is the dielectric constant of the substrate. Hence, for a side length of 9 mm, the antenna resonates at 2.4 GHz. Now, in configuration B, a vertical arm is introduced at the center which in turn is connected to the feed directly. This vertical arm, opens up the higher order resonance. Finally, in configuration C, a split is introduced at the center of the vertical arm, which in turn opens up the quarter wave resonance corresponding to length L_1 and also, induces a narrow magnetic resonance due to its capacitive effect and creates a sharp notch corresponding to the split width, yielding two resonant bands centered at 2.4 GHz and at 6 GHz. A detailed layout of the proposed antenna is shown in Fig. 2 along with its side view and its dimensions are listed in Table 2. Photograph of the proposed structure is shown in Fig. 3.

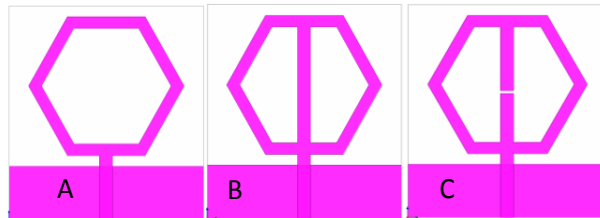


Fig. 1. Evolution of the proposed antenna.

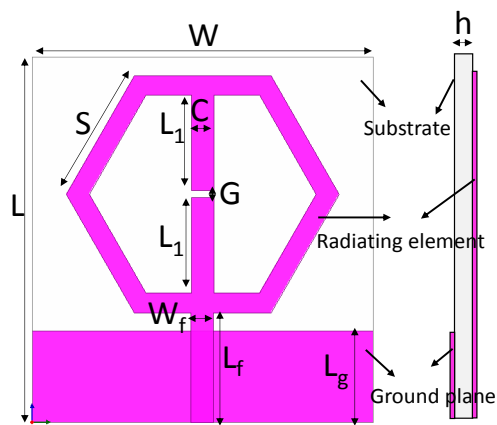


Fig. 2. Geometry of the proposed antenna: (a) top view and (b) side view.

Table 2: Dimensions of the proposed antenna

Parameter	Dimension (mm)	Parameter	Dimension (mm)
L	24	W	22.5
S	9	C	1.5
G	0.3	L_1	6.3
L_f	7.2	W_f	1.5
L_g	6	h	0.8

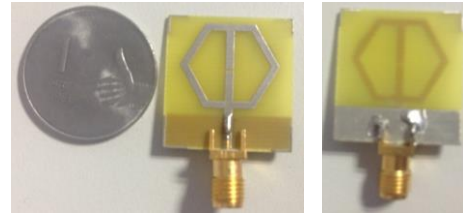


Fig. 3. Photograph of the fabricated dual band antenna (top view and bottom view).

III. SIMULATION RESULTS

Simulations are performed using the Ansoft High Frequency Structure Simulator (HFSS) V.15.0 commercial software package. Figure 4 shows the simulated return loss characteristics of three configurations shown in Fig. 1. Configuration A shows resonance around 2.4 GHz. When the vertical arm is introduced (configuration B), a higher order resonance is noted. The width of the vertical arm plays an important role in determining the higher order resonance. Finally, in configuration C, a split is introduced at the center of the vertical arm to induce magnetic resonance. Now, the higher order resonance is opened from 4 GHz to 7.5 GHz, covering the upper WLAN frequencies (5.15–5.35) and (5.75–5.825). Figure 5 shows the parametric study on the return loss characteristics of configuration C for various vertical arm's width C , ranging from 1.5 mm to 6 mm in steps of 1.5 mm. It is inferred that, as the width C increases, the notch frequency is shifted towards the lower frequencies, opening the upper WLAN band. The lower frequency limit of this band (5.2/5.8 GHz) is determined by the dimension $L_1 \times C$. For $L_1 = 6.3$ mm and $C = 1.5$ mm, the lower frequency limit is the quarter wave resonance of length (6.3 mm + 1.5 mm). Thus, $C = 1.5$ mm is chosen to be optimum for our design, which corresponds to the notch around 4 GHz. It is also inferred that, for $C = 6$ mm, the WiMAX band (3.5 GHz) is also covered.

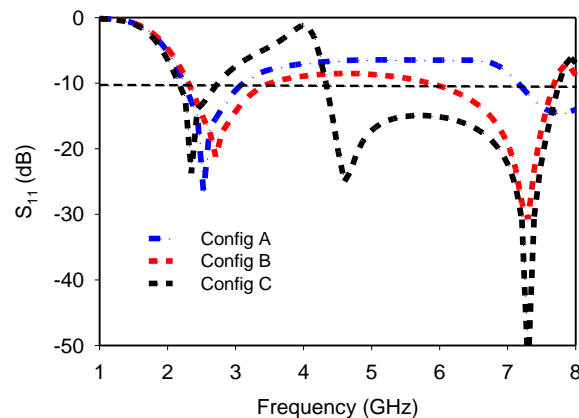


Fig. 4. Simulated return loss characteristics of the three configurations A, B, and C.

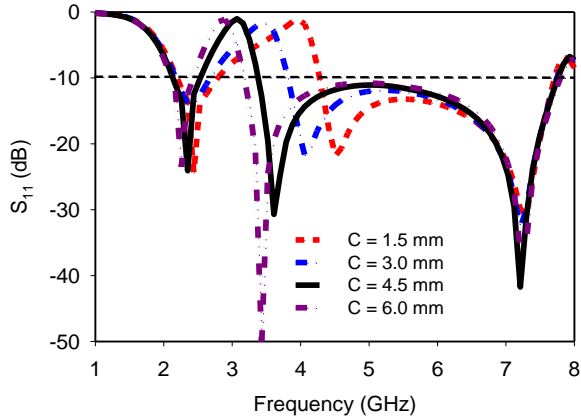


Fig. 5. Simulated return loss characteristics of configuration C for various width G.

Similarly, the split gap G plays an important role in determining the notch frequency. Figure 6 shows the parametric study on the return loss characteristics of configuration C for various split width G ranging from 0.3 mm to 0.9 mm in steps of 0.2 mm. It is observed that, as the split gap G increases, the notch frequency also increases correspondingly. Hence, G = 0.3 mm is chosen for our design, for a notch to occur around 4 GHz.

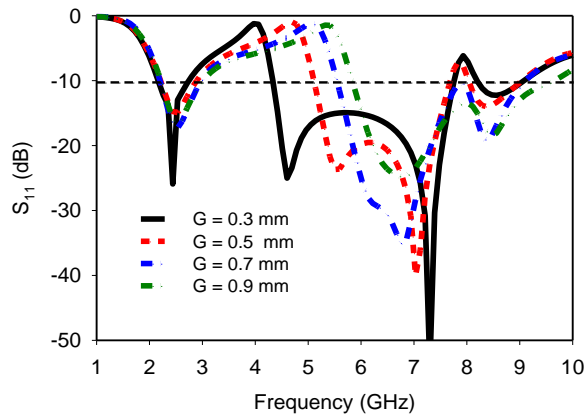


Fig. 6. Simulated return loss characteristics of configuration C for various width G.

IV. SPLIT RING ANALYSIS

The radiating element is itself a split ring structure which is analyzed using the classic waveguide theory approach. The transmission and reflection coefficients are noted and from which the effective material parameters, permeability and permittivity are extracted. Figure 7 shows the real parts of extracted effective permeability values plotted along with the return loss characteristics of the proposed structure. It is inferred that the permeability is negative around 4 GHz. This

negative permeability region has in turn led to the notch frequency, which can be clearly understood by the dashed grey region. Due to the negative permeability, no transmission is practical in this region, thus the S_{11} curve exhibits notch band over this region.

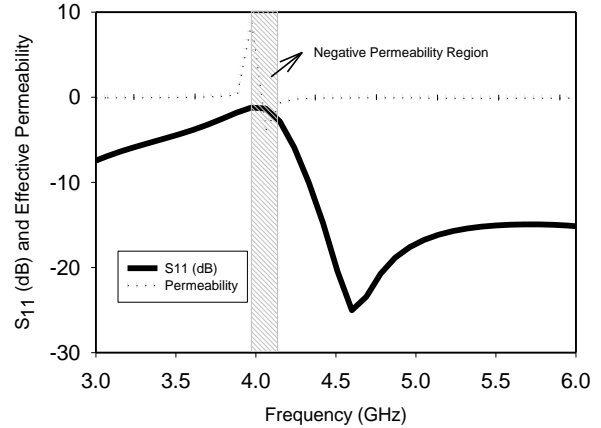


Fig. 7. Comparison of extracted real parts of effective permeability and S_{11} (dB).

V. MEASUREMENT RESULTS

The return loss characteristics are measured using a vector network analyzer. Figure 8 shows the simulated and measured return loss results. The measured data shows dual band resonance centered at 2.4 GHz (2.0 – 2.7 GHz) and at 4.4 GHz and 7.12 GHz (4.12 – 7.66 GHz). The measured data greatly agree with the simulated results. The radiation pattern of the proposed antenna is measured in an anechoic chamber, which is shown in Fig. 9. A consistent omnidirectional pattern is observed in the H plane and a bidirectional pattern is observed in the E plane over all the operating region (2.4, 5.5 GHz).

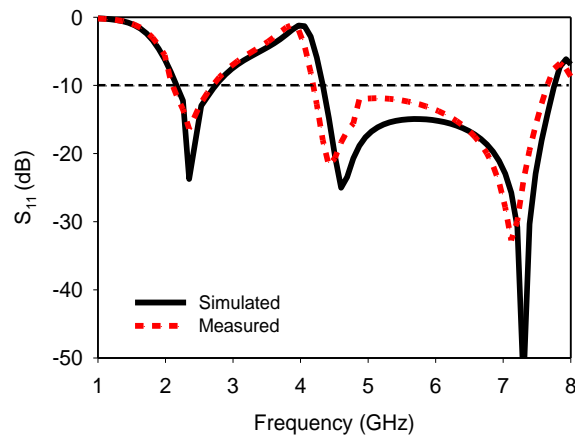


Fig. 8. Simulated and measured return loss characteristics of the proposed antenna.

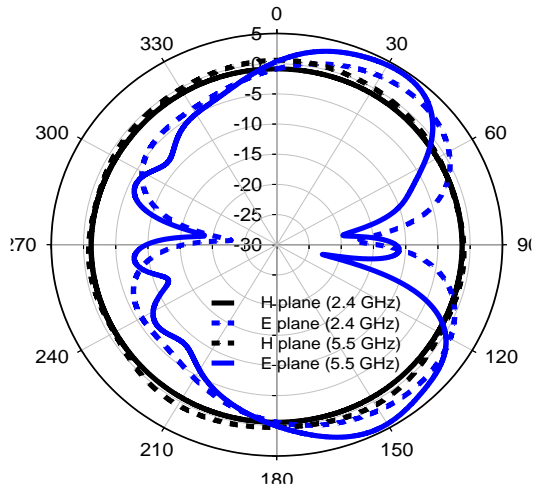


Fig. 9. Measured H plane and E plane pattern of the proposed antenna at 2.4 GHz and 5.5 GHz.

VI. CONCLUSION

A dual band monopole antenna suitable for WLAN 2.4/5.5 GHz applications is presented in this paper. The antenna makes use of a metamaterial inspired split ring structure for achieving the dual band resonance. The antenna geometry is very simple and also compact making mass production easy. The radiation pattern and gain are consistent over all the operating bands making the proposed antenna a good choice for wireless applications.

REFERENCES

- [1] Y. Xu, Y.-C. Jiao, and Y.-C. Luan, "Compact CPW-fed printed monopole antenna with triple band characteristics for WLAN/WiMAX applications," *Electron Lett.*, vol. 48, pp. 1519-1520, 2012.
- [2] X. L. Sun, L. Liu, S. W. Cheung, and T. I. Yuk, "Dual-band antenna with compact radiator for 2.4/5.2/5.8 GHz WLAN applications," *IEEE Trans. Ant. P.*, vol. 60, pp. 5924-5931, 2012.
- [3] W.-C. Liua, C.-M. Wua, and N.-C. Chu, "A compact low profile dual-band antenna for WLAN and WAVE applications," *AEU Int. J. Electron. C.*, vol. 66, pp. 467-471, 2012.
- [4] C.-Y. Huang and E.-Z. Yu, "A slot monopole antenna for dual band WLAN applications," *IEEE Antennas Wireless Propag. Lett.*, vol. 10, pp. 500-502, 2011.
- [5] X.-Q. Zhang, Y.-C. Jiao, and W.-H. Wang, "Compact wide tri-band slot antenna for WLAN/WiMAX applications," *Electron. Lett.*, vol. 48, pp. 64-65, 2012.
- [6] H.-Y. Chien, C.-Y.-D. Sim, and C.-H. Lee, "Dual band meander monopole antenna for WLAN operation in laptop computer," *IEEE Antennas Wireless Propag. Lett.*, vol. 12, pp. 694-697, 2013.
- [7] R. Ghatak, R. K. Mishra, and D. R. Poddar, "Perturbed Sierpinski carpet antenna with CPW feed for IEEE 802.11 a/b WLAN application," *IEEE Antennas Wireless Propag. Lett.*, vol. 7, pp. 742-744, 2008.
- [8] D. Laila, R. Sujith, V. A. Shameena, C. M. Nijas, V. P. Sarin, and P. Mohanan, "Complementary split ring resonator-based microstrip antenna for compact wireless applications," *Microw. Opt. Technol. Lett.*, vol. 55, pp. 814-816, 2013.
- [9] R. O. Ouedraogo, E. J. Rothwell, A. R. Diaz, K. Fuchi, and A. Temme, "Miniaturization of patch antennas using a metamaterial-inspired technique," *IEEE Trans. Ant. P.*, vol. 60, pp. 2175-2182, 2012.
- [10] Y. H. Xie, C. Zhu, L. Li, and C. H. Liang, "A novel dual-band metamaterial antenna based on complementary split ring resonators," *Microw. Opt. Technol. Lett.*, vol. 54, pp. 1007-1009, 2012.
- [11] L.-W. Li, Y.-N. Li, T. S. Yeo, J. R. Mosig, and O. J. F. Martin, "A broadband and high-gain metamaterial microstrip antenna," *Appl. Phys. Lett.*, vol. 96, pp. 164101-164103, 2010.
- [12] S. C. Basaran and Y. E. Erdemli, "A dual band split ring monopole antenna for WLAN applications," *Microw. Opt. Technol. Lett.*, vol. 51, pp. 2685-2688, 2009.
- [13] S. C. Basaran, U. Olgun, and K. Sertel, "Multiband monopole antenna with complementary split ring resonators for WLAN and WiMAX applications," *Electron. Lett.*, vol. 49, pp. 636-638, 2013.
- [14] K. Yang, H. Wang, Z. Lei, Y. Xie, and H. Lai, "CPW-fed slot antenna with triangular SRR terminated feed line for WLAN/WiMAX applications," *Electron. Lett.*, vol. 47, pp. 685-686, 2011.
- [15] C. A. Balanis, *Antenna Theory: Analysis and Design*. John Wiley & Sons, 2005.

The Equivalent Circuit Extraction and Application for Arbitrary Shape Graphene Sheet

Ying S. Cao¹, Li Jun Jiang¹, and Albert E. Ruehli²

¹Department of Electrical and Electronic Engineering
The University of Hong Kong, Pokfulam Road, Hong Kong
caoying@eee.hku.hk, jianglj@hku.hk

²UMRI/MST EMC Laboratory
Missouri University of Science and Technology, Rolla, MO 65409, USA
albert.ruehli@gmail.com

Abstract — In this work, for the first time the electromagnetic features of graphene are characterized by a circuit model derived instead of fitted from the electric field integral equation (EFIE). The atomically thick graphene is equivalently replaced by an impedance surface. When it is magnetized, the impedance surface is anisotropic with a tensor conductivity. Based on EFIE, the graphene's circuit model can be derived by the partial element equivalency circuit (PEEC) concept. The anisotropic resistivity is modeled using a serial resistor with current control voltage sources (CCVSs). From the derived circuit model, electromagnetic properties of graphene can be conveniently analyzed. This work also provides a new characterization method for dispersive and anisotropic materials.

Index Terms — Graphene, magnetized, non-magnetized, PEEC.

I. INTRODUCTION

Graphene is an atomically thin nanomaterial with promising application potentials. However, its electromagnetic modeling is usually totally numerical [1] or physically empirical. This fact motivated us, in this paper, to derive an equivalent circuit model based on EFIE for both non-magnetized and magnetized graphene. It employs the PEEC [2-7] process to convert the electromagnetic interactions on the graphene surface into resistive, inductive and capacitive effects on an isotropic or anisotropic impedance surface. By solving the derived circuit model, graphene's electromagnetic properties can be fully predicted conveniently and efficiently.

In this paper, a novel circuit model based on the electric field integral equation (EFIE) is proposed to solve the dispersivity of non-magnetized and magnetized graphene. For the non-magnetized graphene, the conductivity is composed of intraband and interband

contributions. The resistive part in the equivalent circuit model is modeled as a resistor, an inductor and they are in series with Zinter which accounts for the interband contribution of the surface conductivity of graphene. In the equivalent circuit model for magnetized graphene, the diagonal elements of the surface conductivity tensor intrinsically correspond to the resistance of each inductive branch, which is the same as the unbiased scalar conductivity of graphene. For the off-diagonal elements of the conductivity tensor, a new equivalent circuit model is developed to model the resistive characteristics by utilizing current-controlled voltage sources (CCVSs).

The advantages of the proposed new method are: (i) The model is derived based on EM wave equations. It is not empirical or curve fitted. Hence, it is more reliable and general. Based on our search, this is the first derived model for graphene. (ii) The new method is much more efficient than the volumetric based graphene modeling process. (iii) Compared with the numerical process [8], the derived circuit model of graphene provides a convenient bridge to integrate graphene EM parasitic effects with lumped circuit designs.

II. EQUIVALENT CIRCUIT MODEL DERIVATION FOR GRAPHENE

The 2D atomically thin graphene can be considered as an impedance surface with the dispersive conductivity that is isotropic or anisotropic along tangential directions [9]. Based on the electric field integral equation, we have:

$$\mathbf{E}^{inc}(\mathbf{r}, t) = \frac{\mathbf{J}(\mathbf{r}, t)}{\sigma} + \mu \int_{v'} G(\mathbf{r}, \mathbf{r}') \frac{\partial \mathbf{J}(\mathbf{r}', t)}{\partial t} dv' + \frac{\nabla}{\epsilon} \int_{v'} G(\mathbf{r}, \mathbf{r}') q(\mathbf{r}', t) dv', \quad (1)$$

where $G(\mathbf{r}, \mathbf{r}')$ is the full wave Green's function. For one current filament on the graphene sheet, using the partial equivalence element concept, Eq. (1) becomes Kirchhoff's

Voltage Law:

$$V = RI + Lp \frac{dI}{dt} + Q \cdot Pp, \quad (2)$$

where Lp is the partial inductance, and Pp is the partial coefficient of potential. The Lp between cell α and β and Pp between cell i and j are:

$$Lp_{\alpha\beta} = \frac{\mu}{a_\alpha a_\beta} \int_{v_\alpha} \int_{v_\beta} G(\mathbf{r}_\alpha, \mathbf{r}_\beta) dv_\alpha dv_\beta, \quad (3)$$

$$Pp_{ij} = \frac{1}{\varepsilon S_i S_j} \int_{S_i} \int_{S_j} G(\mathbf{r}_i, \mathbf{r}_j) dS_i dS_j. \quad (4)$$

The 2-dimensional meshing scheme can be represented as Fig. 1 [2].

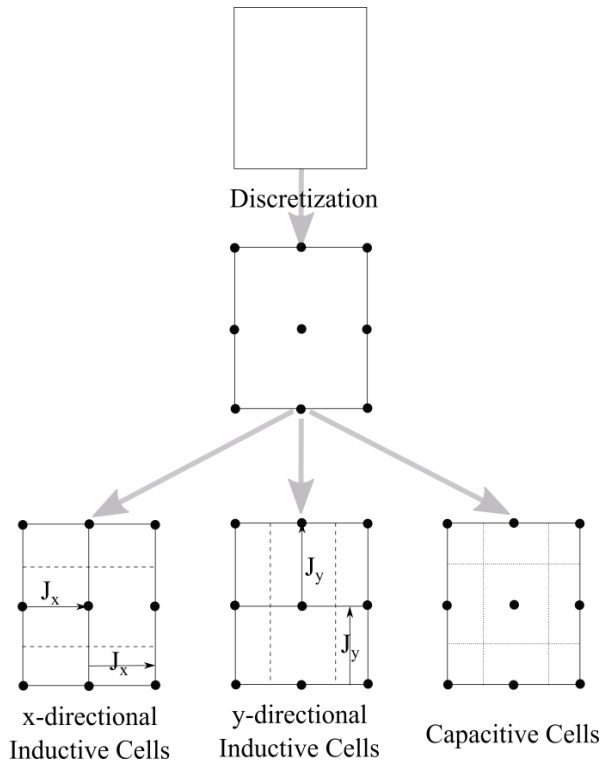


Fig. 1. This is the 2D discretization of thin conductive plate. Dark circles indicate nodes, dashed lines separate inductive cells, and dotted lines separate capacitive cells.

A. Non-magnetized graphene

The graphene dispersive conductivity σ is a summation of both intraband and interband contributions [10]. For a one freestanding rectangular patch with the length l and width w , its surface resistance can be derived from Kubo's formula:

$$R_{surf} = R_r + j\omega L_r + Z_{inter}, \quad (5)$$

where R_r is from the real part of σ , L_r is from the imaginary part of σ , and Z_{inter} is from the inter band part.

Combining other parts of the cell model, the new non-magnetized graphene unit model is illustrated in Fig. 2.

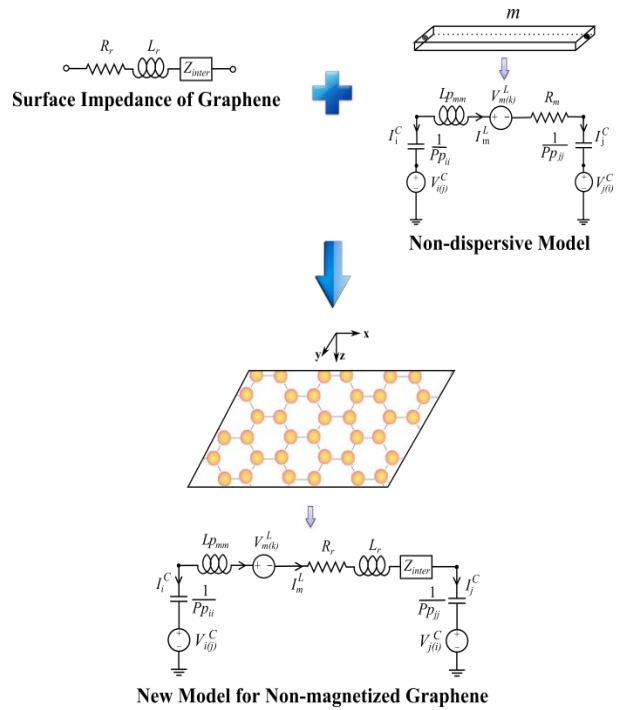


Fig. 2. One cell's model for a non-magnetized graphene patch. The left bottom model is the traditional equivalent model, where Lp_{mm} , Pp_{ii} and Pp_{ij} are self-inductance and self-coefficients of potential, respectively. $V_{m(k)}^L$ is the voltage control voltage source (VCVS) corresponding to mutual inductive couplings. $V_{i(j)}^C$ and $V_{j(i)}^C$ are the voltage control voltage sources (VCVSs) due to mutual capacitive coupling between two capacitors i and j .

B. Magnetized graphene

With the bias by a static magnetic field, the surface conductivity of graphene becomes an anisotropic tensor, which complicates the problem. Hence, the numerical methods have to settle the dispersive and anisotropic properties of graphene simultaneously.

For the magnetized graphene, its surface conductivity becomes an anisotropic and dispersive tensor $\bar{\sigma}$ [9]. Hence, the electric field has contributions from orthogonal current components. For example, the x-direction electric field is a function of J_x and J_y . Hence, for off-diagonal elements of the conductivity tensor, a current control voltage source (CCVS) can be used to represent each of these orthogonal contributions. CCVSs are in series with the intrinsic resistances that are derived from diagonal terms of $\bar{\sigma}$. In Fig. 3, the new equivalent circuit model for the magnetized graphene is sketched.

$$\begin{aligned} \mathbf{E}^{tot} &= \mathbf{E}^{inc} - \frac{\partial \mathbf{A}}{\partial t} - \nabla \phi = \boldsymbol{\sigma}^{-1} \mathbf{J} = \boldsymbol{\rho} \mathbf{J} \\ &= (\rho_{xx} J_x + \rho_{xy} J_y) \hat{x} + (\rho_{yx} J_x + \rho_{yy} J_y) \hat{y} \end{aligned}$$

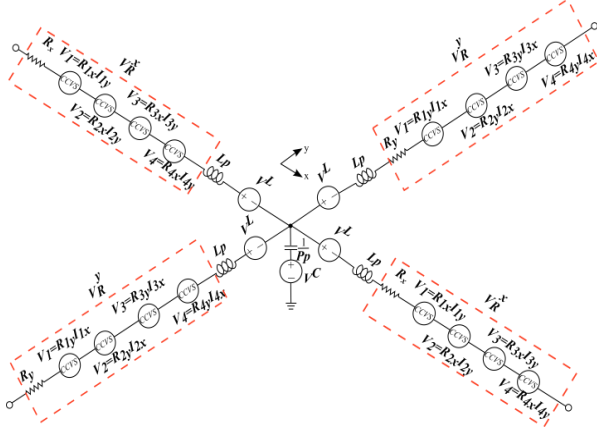


Fig. 3. A schematic diagram of the complete equivalent circuit for magnetized anisotropic conductivity graphene. This circuit model is for four nearby cells which share a common node, and two for x-directional cells and the other two for y-directional cells. The scripts for each cell are omitted for simplicity.

III. NUMERICAL RESULTS

A. Non-magnetized graphene

The $5 \times 0.5 \mu\text{m}^2$ graphene patch is illuminated by a plane wave linearly polarized along the patch length. The direction of propagation is normal to the surface of graphene. The absorption cross section of the graphene patch is shown in Fig. 4 for different relaxation times. By comparing with results from [10] (represented by circles), it is seen that perfect agreements are achieved including the positions of important resonant frequencies.

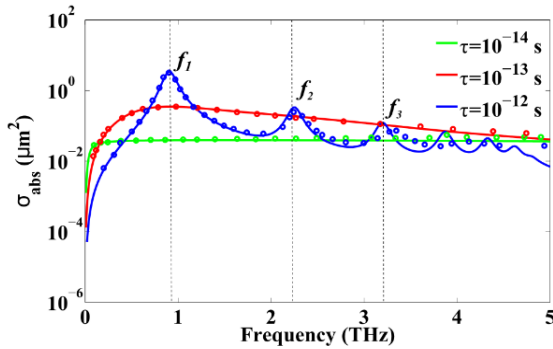


Fig. 4. Absorption cross section (in logarithmic scale) of a non-magnetized graphene patch as a function of frequency, for different relaxation time: 10^{-14} s (green line), 10^{-13} s (red line), 10^{-12} s (blue line). The results are compared with [5] plotted using circles. f_1 , f_2 and f_3 are resonant frequencies.

B. Magnetized graphene

To validate the accuracy of the proposed algorithm for the magnetized graphene, a $10 \times 2 \mu\text{m}^2$ graphene patch is studied first. Relaxation time $t = 1.3 \times 10^{-13}$ s. The magnetic bias $B_0 = 0.25$ T. The graphene patch is biased by a z-directional static magnetic field and the same excitation plane wave in III.A is used. The absorption cross section and extinction cross section calculated by new method and discontinuous Galerkin method [9] are compared in Fig. 5. The definitions of the absorption cross section and extinction cross section can be found in [6].

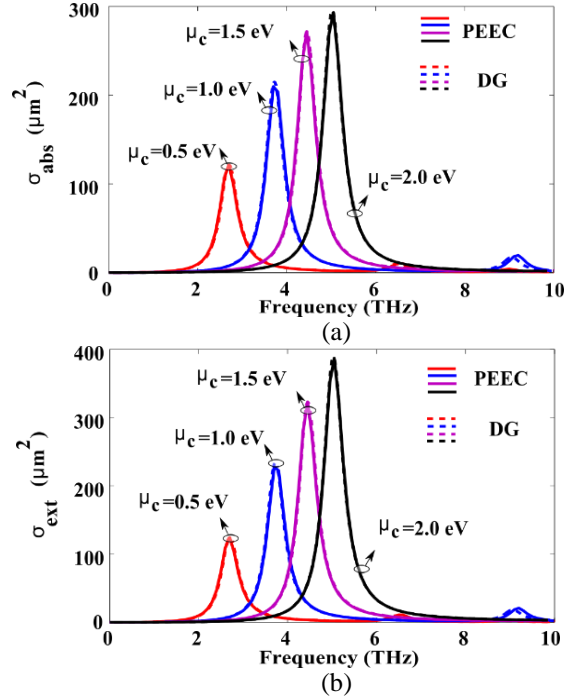


Fig. 5. (a) σ_{abs} (absorption cross section) and (b) σ_{ext} (extinction cross section) of the magnetized graphene patch.

IV. CONCLUSION

In this paper, a novel equivalent circuit model is derived for the general graphene sheet based on EM integral equations. It provides a new bridge between EM parasitic effects and lumped circuit designs for researches on graphene and other dispersive anisotropic media.

ACKNOWLEDGMENT

This work was supported in part by the Research Grants Council of Hong Kong (GRF 716713, GRF 17207114, and GRF 17210815), NSFC 61271158, and Hong Kong UGC AoE/P-04/08.

REFERENCES

- [1] V. Nayyeri, M. Soleimani, and M. Ramahi, "Wideband modeling of graphene using the finite-difference time-domain method," *IEEE Trans. Antenna Propag.*, vol. 6, no. 12, pp. 6107-6114, Dec. 2013.
- [2] A. E. Ruehli, "Equivalent circuit models for three dimensional multiconductor systems," *IEEE Trans. Microw. Theory Tech.*, vol. MTT-22, no. 3, pp. 216-221, Mar. 1974.
- [3] A. E. Ruehli, "Inductance calculations in a complex integrated circuit environment," *IBM J. Res. Develop.*, vol. 16, no. 5, pp. 470-481, Sep. 1972.
- [4] A. E. Ruehli and P. A. Brennan, "Efficient capacitance calculations for three-dimensional multiconductor systems," *IEEE Trans. Microw. Theory Tech.*, vol. 21, no. 2, pp. 76-82, Feb. 1973.
- [5] Y. S. Cao, L. Jiang, and A. E. Ruehli, "Distributive radiation and transfer characterization based on the PEEC method," *IEEE Trans. Electromag. Compat.*, vol. 57, no. 4, pp. 734-742, Aug. 2015.
- [6] Y. S. Cao, L. Jiang, and A. E. Ruehli, "An equivalent circuit model for graphene-based terahertz antenna using the PEEC method," *IEEE Trans. Antenna Propag.*, vol. 64, no. 4, pp. 1385-1393, Apr. 2016.
- [7] Y. S. Cao, L. Jiang, and A. E. Ruehli, "The derived equivalent circuit model for magnetized anisotropic graphene," submitted to *IEEE Trans. Antenna Propag.*
- [8] O. V. Shapoval, J. S. G.-Diaz, J. P.-Carrier, J. R. Mosig, and A. I. Nosich, "Integral equation analysis of plane wave scattering by coplanar graphene strip gratings in the THz range," *IEEE Trans. Terahertz Sci. Techn.*, vol. 6, no. 3, pp. 666-674, Sept. 2013.
- [9] P. Li and L. J. Jiang, "Modeling of magnetized graphene from microwave to THz range by DGTD with a scalar RBC and an ADE," *IEEE Trans. Antennas Propag.*, vol. 63, no. 10, Oct. 2015.
- [10] I. Llatser, C. Kremers, D. N. Chigrin, J. M. Jornet, M. C. Lemme, A. Cabellos-Aparicio, and E. Alarcon, "Radiation characteristics of tunable graphene as in the terahertz band," *Radioengineering*, vol. 21, no. 4, pp. 946-953, 2012.

A Subwavelength Perfect Absorbing Metamaterial Patch Array Coupled with a Molecular Resonance

Michael F. Finch and Brian A. Lail

Department of Electrical and Computer Engineering
Florida Institute of Technology, 150 West University Blvd., Melbourne, FL, 32901, USA
mfinch2009@my.fit.edu, blail@fit.edu

Abstract — A perfectly absorbing metamaterial (PAMM) coupled with vibrational modes has varied applications ranging from surface-enhanced vibrational spectroscopy to biological sensing. This endeavor considers a subwavelength PAMM sensor design and analysis using a commercially available finite element method (FEM) solver and analytically with temporal coupled mode theory (TCMT). A carbon double oxygen bond (C=O) at 52 THz or 1733 cm^{-1} that resides in poly(methyl methacrylate), PMMA, will be used as a stand-in analyte. Normal mode splitting that results from the resonant coupling between the PAMM and analyte's molecular resonance is investigated and analyzed.

Index Terms — Electromagnetic Induced Absorption (EIA), Electromagnetic Induced Transparency (EIT), metamaterial, perfect absorbing, PMMA, resonant coupling, superscattering.

I. INTRODUCTION

Metamaterial are engineered materials that are designed with periodic or aperiodic elements known as meta-atoms [1]. A perfect absorbing metamaterial (PAMM), as the name implies, is designed to “perfectly” absorb incident fields, and have been described with a metamaterial impedance matched to free space [2-5]. A commercially available finite element method solver, Ansys high frequency structural simulator (HFSS), is employed to design and simulate a gold patch array metasurface with ground plane to form a subwavelength optical resonant cavity.

Resonant coupling results in avoidance crossing dispersion relationships, or normal mode splitting, that is described with temporal coupled mode theory (TCMT) [2, 6-9]. Coupled resonant models have been used a classical analogy treatment of quantum phenomena, namely Fano resonance with bright/dark mode interactions [10-12], and electromagnetically induced transparency or absorption (EIT or EIA) [2, 13-17]. In a Fano resonance, EIT, or EIA treatment a molecular resonance is modeled as a dark mode. TCMT has also

been used to describe light-matter interactions in polaritonic systems [18].

In the case of this work, poly(methyl methacrylate) (PMMA), a thermal plastic for very-large-scale integration (VLSI) and material for plastic fibers, has a carbon double oxygen (C=O) molecular resonance at 52 THz/ 1733 cm^{-1} with optical material properties measured using ellipsometry [19]. PMMA's C=O infrared (IR) active molecular bond will be used as an analyte stand-in to demonstrate the mode splitting. Metamaterial coupled to molecular resonances has varied applications including, but not limited to, biosensing and surface enhanced-vibrational spectroscopy [4, 9, 10, 13, 20, 21].

II. PAMM SENSOR

The PAMM unit cell under consideration is a gold patch stood-off above from a gold ground plane by a spacer of amorphous silicon as shown in Fig. 1. For the preliminary analysis of the PAMM, a thin overlay of material with the refractive index that of dispersionless PMMA is introduced to reduce the red shifting induced on the PAMM's resonance [4]. The PAMM spacer thickness range is on the order of 20 to 200 nm which results in a subwavelength nanoresonator cavity.

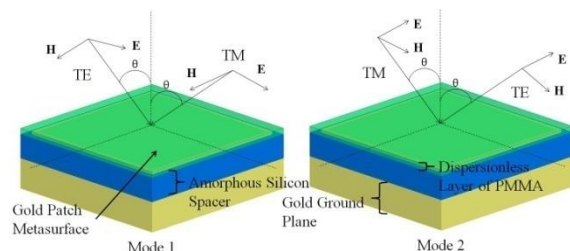


Fig. 1. PAMM unit cell modeled in Ansys HFSS.

A. Theory

Derived from circuit theory or mass spring relationships [2, 6, 21], it can be seen from the TCMT that the PAMM can be modeled as a single input uncoupled system (SI-US) as seen in Fig. 2. The TCMT

equations for normalized resonator energy “ a ” at resonator frequency ω_0 can be written as:

$$\frac{da}{dt} = j\omega_0 a - (\gamma_0 + \gamma_e)a + \alpha S^+, \quad (1.a)$$

$$S^- = cS^+ + da, \quad (1.b)$$

where [2, 6],

$$|\alpha| = \sqrt{2\gamma_e}, \quad (2.a)$$

$$d = \sqrt{2\gamma_e}, \quad (2.b)$$

$$c = -\frac{\alpha}{d} = -1, \quad (2.c)$$

and γ_0 and γ_e represent internal and external losses, respectively. The internal loss can be thought of as Ohmic loss within the PAMM or circuit resonator. External loss results from excitation that does not couple into the PAMM or resonator, but reflects or scatters out of the structure. The excitation and reflected field is denoted as S^+ and S^- respectively.

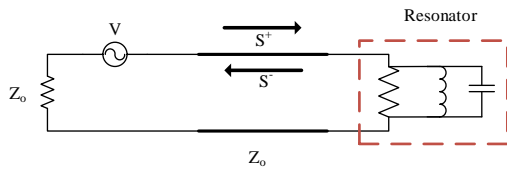


Fig. 2. Circuit visualization for a SI-US where the resonator circuit models the PAMM.

Given the single input description of the PAMM and from (1) and (2) it can be seen that the only scattering parameter is the reflection coefficient:

$$S^- = \left[\frac{j(\gamma_e - \gamma_0) + (\omega - \omega_0)}{j(\gamma_e + \gamma_0) - (\omega - \omega_0)} \right] S^+, \quad (3)$$

and at resonance (3) becomes:

$$S_{11}(\omega_0) = \frac{\gamma_e - \gamma_0}{\gamma_e + \gamma_0}. \quad (4)$$

Due to the ground plane in the PAMM the transmission spectrum can be taken as negligible; therefore,

$$A(\omega) = 1 - |S_{11}(\omega)|^2, \quad (5)$$

where $A(\omega)$ is the absorbed power in the PAMM. It can be seen from (4) when $\gamma_e = \gamma_0$ then $|S_{11}(\omega_0)|$ tends to zero, or $A(\omega)$ becomes unity. The condition $\gamma_e = \gamma_0$ can be described via impedance matching and results in the “perfect absorption” condition in the metamaterial known as criticallycoupled [2, 3, 6]. The condition $\gamma_e < \gamma_0$ and $\gamma_e > \gamma_0$ is referred to as undercoupled and overcoupled respectively. The “coupling” in critically-(CC), under-(UC), and overcoupled (OC) is in reference to the impinging field “coupling” into the PAMM and not related to the molecular resonance.

B. PAMM numerical results

While maintaining the PAMM at approximately at 52 THz (molecular resonant frequency), the thickness of the A-Si spacers was varied. A case of OC, CC, and UC can be seen in Fig. 3 for spacer thickness of 150, 90, and

50 nm respectively. From (4), it can be seen that the CC case is the only case where approximately the perfect absorption condition is met. Figure 4 is the spectral and angular resolution for the absorption for the CC case for both incident modes seen in Fig. 1. It can be seen that the design patch metamaterial provides a polarization insensitive to transverse electrical (TE), transverse magnetic (TM), or either mode orientation while providing a wide-field-of-view [3]. With the use of the TCMT equations, the damping rates, external (γ_e) and internal (γ_0), were determined by a parametric fit and the absorption is plotted in Fig. 3 as seen as asterisks (*), and linear fit as seen in Fig. 5.

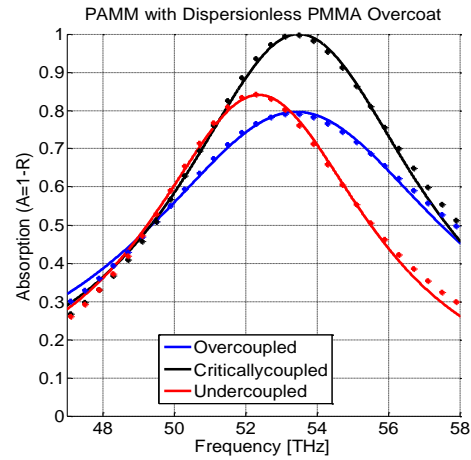


Fig. 3. Numerical (*) and mathematical model (solid line) results are shown for case of over-(OC), critically-(CC), and undercoupled (UC) cases.

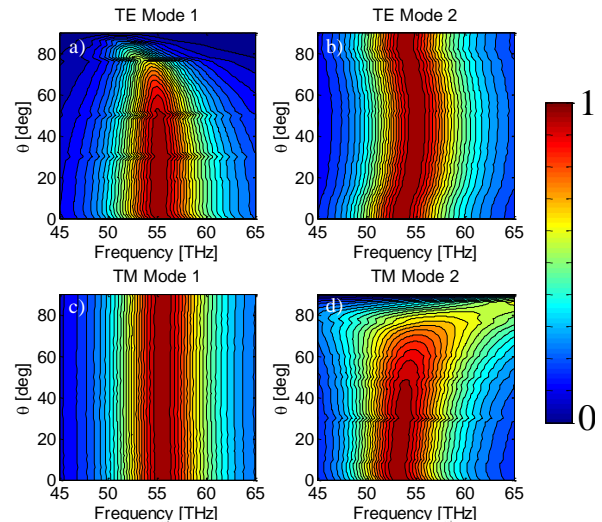


Fig. 4. Absorption spectra and angular-resolved for the criticallycoupled cases as seen in Fig. 1. Both TE (a, b) and TM (c, d) polarizations are shown for both mode orientations.

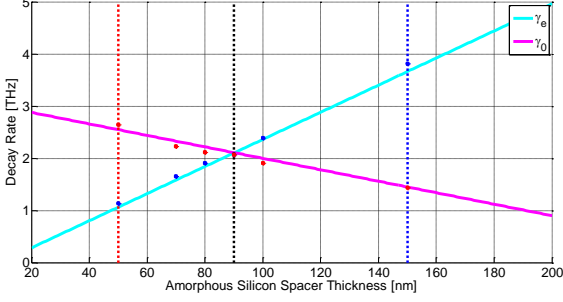


Fig. 5. Linear relationship between external (γ_e) and internal (γ_0) loss as a function of amorphous space thickness. CC case is seen at around 90 nm Si spacer thickness.

III. PAMM-MOLECULAR COUPLING

A. TCMT description

Similar to a EIT/EIA or Fano resonant description, the molecular resonance is a weak coupling to the incident field and is a spectrally narrow resonance, therefore; it can be model as a dark resonance mode [2, 10, 12, 13] as seen in the circuit realization in Fig. 6. However, the PAMM provides a spectrally broad resonance and couples very strongly with the incident field, and thus can be thought as a bright mode as seen in Fig. 6.

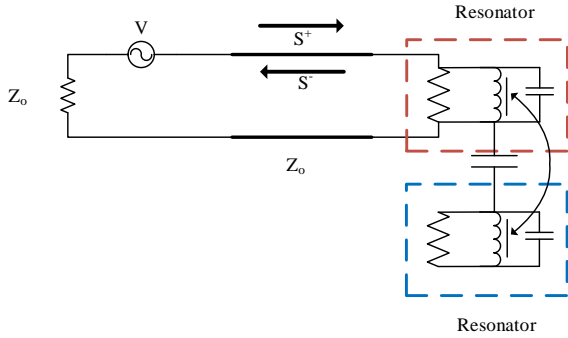


Fig. 6. Circuit visualization for a single input coupled resonator system.

Using TCMT, an additional equation describing the molecule resonance, “ a_2 ”, with complex frequency $\omega_2 + j\gamma_2$. The interaction or mode coupling between the PAMM and molecule resonance is described with the coupling strength “ V ”. The coupling strength is a result of the interactions of the near field from the PAMM on to the PMMA molecular bond. The TCMT system of equations that results are as follows [2, 18]:

$$\frac{da_1}{dt} = j\omega_1 a_1 - (\gamma_1 + \gamma_e) a_1 + jV a_2 + \alpha S_1^+, \quad (6.a)$$

$$\frac{da_2}{dt} = j\omega_2 a_2 - \gamma_2 a_2 + jV a_1, \quad (6.b)$$

$$S^- = cS^+ + da_1. \quad (6.c)$$

B. PAMM molecular resonance coupled numerical results

With the introduction of the PMMA phonon resonance, it can be observed that for the CC and UC cases in mode splitting or EIT [12, 14] while OC case results in superscattering or EIA [15, 16] as seen in Figs. 7 and 8. Figure 8 (b) shows the avoided crossing dispersion relation [8] where the variation of the only the A-Si spacer thickness resulting in changing the PAMM resonances or absorption maximum spectrally.

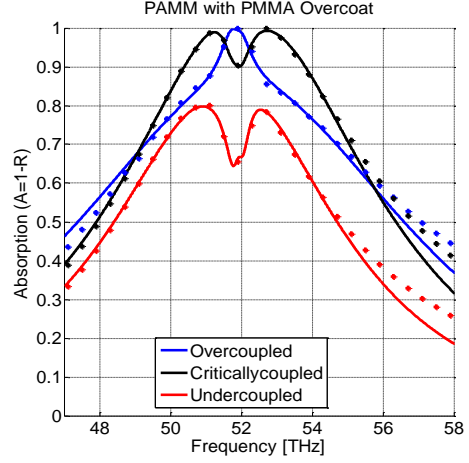


Fig. 7. Numerical (*) and mathematical model (solid line) results are shown for resonant coupling between PAMM and molecular resonance.

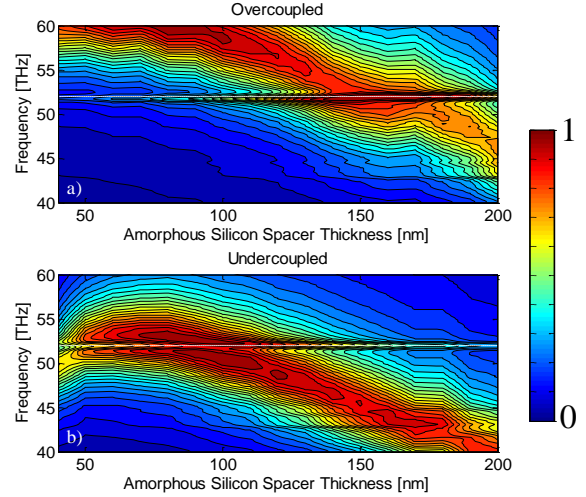


Fig. 8. Absorption spectra for PAMM resonantly coupled to a molecular resonance at 52 THz (white dashed line) for OC (a) and UC (b) cases for varying A-Si spacer thickness.

IV. CONCLUSION

With the use of finite element method and TCMT, a perfect absorbing patch metamaterial resonant coupled

to a C=O doubled bond at 52 THz of PMMA was investigated. EIT and EIA responses and anti-crossing dispersion are evident when resonated couple between a PAMM and molecule resonance is presented.

REFERENCES

- [1] A. V. K., A. Boltasseva, and V. M. Shalaev, "Planar photonics with metasurfaces," *Science*, vol. 339, no. 6125, pp. 1232009-1-1232009-6, 2013.
- [2] R. Adato, A. Artar, S. Erramilli, and H. Altug, "Engineered absorption enhancement and induced transparency in coupled molecular and plasmonic resonator systems," *Nano Letters*, vol. 13, no. 6, pp. 2584-2591, May 2013.
- [3] C. Wu, B. Neuner, and G. Shvets, "Large-area, wide-angle, spectrally selective plasmonic absorber," *Physical Review B*, vol. 84, no. 7, pp. 075105:1-7, August 2011.
- [4] K. Chen, R. Adato, and H. Altug, "Dual-band perfect absorber for multispectral plasmon-enhanced infrared spectroscopy," *ACS Nano*, vol. 6, no. 9, pp. 7998-8006, August 2012.
- [5] N. I. Landy, S. Sajuyigbe, J. J. Mock, D. R. Smith, and W. J. Padilla, "Perfect metamaterial absorber," *Physical Review Letters*, vol. 100, no. 20, pp. 207402-207408, May 2008.
- [6] H. A. Haus, *Waves and Fields in Optoelectronics*. Englewood Cliffs, NJ: Prentice-Hall, Inc., 1984.
- [7] H. A. Haus and W. Huang, "Coupled-mode theory," *Proceeding of the IEEE*, vol. 79, no. 10, pp. 1505-1518, 1991.
- [8] L. Novotny, "Strong coupling, energy splitting, and level crossings: A classical perspective," *American Journal of Physics*, vol. 78, no. 11, pp. 1199-1202, 2010.
- [9] S. Savasta, et al., "Nanopolaritons: Vacuum Rabi splitting with a single quantum dot in the center of a dimer nanoantenna," *ACS Nano*, vol. 4, no. 11, pp. 6369-6376, 2010.
- [10] C. Wu, et al., "Fano-resonant asymmetric metamaterials for ultrasensitive spectroscopy and identification of molecular monolayers," *Nature Materials*, vol. 11, pp. 69-75, January 2012.
- [11] B. Luk'yanchuk, et al., "The Fano resonance in plasmonic nanostructures and metamaterials," *Nature Materials*, vol. 9, pp. 707-715, 2010.
- [12] A. B. Khanikaev, C. Wu, and G. Shvets, "Fano-resonant metamaterials and their applications," *Nanophotonics*, vol. 2, no. 4, pp. 247-264, 2013.
- [13] R. Adato, S. Aksu, and H. Altug, "Engineering mid-infrared nanoantennas for surface enhanced infrared absorption spectroscopy," *Materials Today*, vol. 00, no. 00, pp. 1-11, March 2015.
- [14] C. L. Garrido Alzar, M. A. G. Martinez, and P. Nussenzveig, "Classical analog of electromagnetically induced transparency," *American Journal of Physics*, vol. 70, no. 1, pp. 37-41, 2002.
- [15] X. Zhang, et al., "Electromagnetically induced absorption in a three-resonator metasurface system," *Scientific Reports*, vol. 5, no. 10737, pp. 1-9, May 2015.
- [16] W. Wan, W. Zheng, Y. Chen, and Z. Liu, "From Fano-like interference to superscattering with a single metallic nanodisk," *Nanoscale*, vol. 6, no. 15, pp. 9093-9102, May 2014.
- [17] A. Lovera, B. Gallinet, P. Nordlander, and O. J. F. Martin, "Mechanisms of Fano resonances in coupled plasmonic systems," *ACS Nano*, vol. 7, no. 5, pp. 4527-4536, April 2013.
- [18] S. Zanotto, et al., "Perfect energy-feeding into strongly coupled systems and interferometric control of polariton absorption," *Nature Physics*, vol. 10, no. 11, pp. 830-834, August 2014.
- [19] J. Ginn, et al., "Characterizing infrared frequency selective surfaces on dispersive media," *ACES Journal*, vol. 22, no. 1, pp. 184-188, March 2007.
- [20] T. Chen, S. Li, and H. Sun, "Metamaterials application in sensing," *Sensors*, vol. 12, no. 3, pp. 2742-2765, February 2012.
- [21] D. J. Shelton, et al., "Strong coupling between nanoscale metamaterials and phonons," *Nano Letters*, vol. 11, no. 5, pp. 2101-2108, April 2011.

Unmanned Aerial Vehicle Platform Stabilization for Remote Radar Life Sensing

Robert H. Nakata, Brian Haruna, Scott K. Clemens, Daren Martin, Charles Jaquiro, and Victor M. Lubecke

Department of Electrical Engineering
University of Hawaii at Manoa, Honolulu, HI 96816, USA
rnakata6@hawaii.edu

Abstract — Unmanned Aerial Vehicle (UAV) platforms are increasingly ubiquitous and an ideal platform for rapid deployment to conduct remote sensing. However, for radar sensors that measure the phase of the signal of interest, the platform must be stabilized to avoid signal distortion. Measurement of respiratory motion with a continuous wave Doppler radar sensor is vulnerable to platform motion and requires a stable platform and post-detection motion compensation signal processing. We have investigated feedback stabilization techniques via simulation and empirical measurements using a bench top test fixture to remove the motion noise, where we observed a 86% reduction in motion, resulting in a SNR improvement of 29 dB after motion compensation.

Index Terms — Motion compensation, radar, remote sensing, UAV.

I. INTRODUCTION

Unmanned Aerial Vehicles (UAVs) have the potential for post-disaster search and rescue missions where triage can be conducted on victims using an on-board radar sensor to detect respiratory motion [1].

Vital signs measurements using a stationary Continuous Wave (CW) Doppler radar sensor have been previously demonstrated [2]. Since the signal corresponds to the phase modulation resulting from the range variation between the radar and the subject, any sensor platform motion will induce an undesired phase component to the respiration signal. Other papers describe motion cancellation techniques for vital signs sensing when the subject motion interferes with the measurement [3]. For our scenario, the assumption is that the subject is stationary as is likely the case for a post-disaster scenario where victims are prone on the ground.

Our hypothesis is that the combination of mechanically stabilizing the platform in conjunction with baseband signal processing will improve the SNR

of the target signal and improve the probability of detection. The concept is similar to camera stabilization systems that apply vibration reduction and pixel shifting to de-blur images resulting from camera shake.

In this paper, we describe the concept of operations (CONOPS) for a UAV post-disaster search platform, platform motion compensation architecture and experimental results for ultrasonic sensor driven motion compensation. A programmable bench top test platform was constructed to mimic the unwanted UAV platform motion. A motion compensation sub-platform was mounted on the base platform and was programmed to compensate for the base platform motion based on inputs from an ultrasonic sensor that measured the unwanted motion in real-time. A 10 GHz radar sensor was mounted on the bench top test platform and pointed at a respiration phantom to assess the performance with and without the motion compensation.

In the following sections, we describe the CONOPS, the motion analysis, simulation, experiment, ultrasonic ranging sensor and experimental results.

II. CONCEPT OF OPERATIONS

The operational concept is for the system to have a search mode, a platform stabilization and signal acquisition mode as shown in Fig. 1. In the search mode, the UAV navigates to the area of interest using GPS waypoint coordinates or could navigate autonomously. An onboard camera with image recognition could be used to identify potential victims (targets) [4, 5]. In the stabilization mode, a suite of sensors, including GPS, IMU, LIDAR and/or ultrasonic range sensors, are used to adjust the UAV Electronic Speed Controllers (ESC) to maintain a steady altitude and fixed Yaw, Pitch and Roll (YPR) attitude. In the platform stabilization mode, the UAV hovers above the subject and uses the stabilization techniques described in this paper to improve the target SNR.

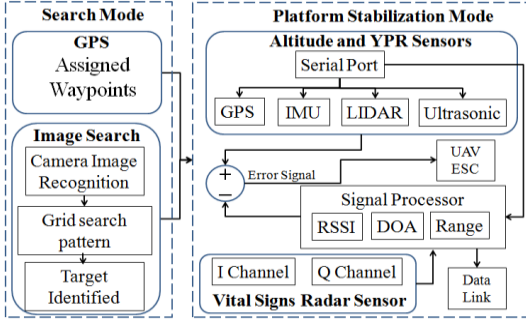


Fig. 1. System block diagram for the search and stabilization modes for the UAV radar sensor platform. Conventional sensors (GPS, IMU, barometric sensors) that determine altitude and yaw, pitch, roll (YPR) are supplemented with range sensors (ultrasonic, LIDAR) for motion compensation. The SNR of the on-board vital signs radar sensor pointed downward is improved by the platform stabilization and post detection baseband signal processing.

III. MOTION ANALYSIS, SIMULATION AND EXPERIMENT

A. Motion analysis

The time domain representations for the respiration signal of interest (modeled as a sinusoid for simplicity) and platform motion components are:

$$\text{respiration signal: } x_1(t) = A \sin(\omega_1 t), \quad (1)$$

$$\text{UAV motion: } x_2(t) = \sin(\omega_2 t). \quad (2)$$

The motion compensation signal $x_3(t)$ is derived from the secondary sensors on board the UAV including the inertial measurement unit IMU(t), ultrasonic sensor U(t) and lidar sensor L(t) with the composite signal represented as:

$$x_3(t) = A * \text{IMU}(t) + B * U(t + \tau_u) + C * L(t + \tau_L), \quad (3)$$

where A, B, C are scaling factors applied to each sensor and τ_i is the sensor signal delay for each sensor i .

The IMU sensor signal is:

$$\text{IMU}(t) = a(t) + m(t) + g(t), \quad (4)$$

where $a(t)$, $m(t)$ and $g(t)$ are the accelerometer, magnetometer and gyroscope signals, respectively.

It should be noted that IMU sensors are subject to position errors due to the double integration operation required to derive position from acceleration. However, the IMU can be used to determine yaw, pitch and roll to determine the platform attitude to account for the offset pointing angle of the ultrasonic and/or LIDAR sensor that are used to determine the range to ground.

The ultrasonic sensor signal is:

$$U(t) = u(t + \phi_u + \tau_u) = x_u(t), \quad (5)$$

the lidar sensor signal is:

$$L(t) = l(t + \phi_L + \tau_L) = x_L(t), \quad (6)$$

and ϕ_i is the measured sensor phase. Note that we explicitly include the sensor phase noise and delays (ϕ_u and τ_u) as these parameters contribute to the phase

compensation error.

As described in the introduction, the range sensor outputs, $x_u(t)$ and $x_L(t)$, can be used to adjust the platform position by providing proportional inputs to the ESC that adjusts the thrust of each motor. Additionally, the same range sensor outputs can be used to extract the platform motion via baseband signal processing.

The motion compensated radar signal $x_1'(t)$ in-phase (I) and quadrature component (Q) include the subtracted sensor phase components as shown below:

$$I = kA \cos[(\omega_1 t) + \phi_r u(t - \phi_u - \tau_u) + l(t - \phi_L - \tau_L)], \quad (7)$$

$$Q = kA \sin[(\omega_1 t) + \phi_r u(t - \phi_u - \tau_u) + l(t - \phi_L - \tau_L)]. \quad (8)$$

B. Motion compensation simulation

A Matlab Simulink program was written to simulate the effect of the UAV platform motion on the respiration signal of interest. An example with sinusoidal respiration and platform motion is shown in Fig. 2.

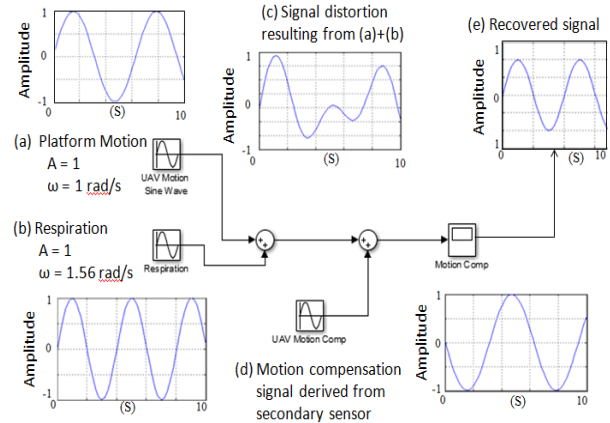


Fig. 2. Motion compensation simulation using Simulink: (a) UAV sinusoidal platform motion at 1 rad/s, (b) respiration sinusoid signal of interest at 1.56 rad/s, (c) motion distortion of signal of interest, (d) motion compensation error signal, and (e) recovered signal.

C. Experiment configuration

The motion compensation experiment block diagram is shown in Fig. 3. The target signal of interest is created with the Mover 1 linear actuator representing a respiration phantom. The UAV platform motion is injected with Mover 2 using a programmable linear actuator from Galil Motion Systems. The motion compensation corrective motion is created with Mover 3. Mover 3 was implemented using a slide potentiometer linear actuator mounted on wheels to allow independent motion from the Mover 2 base platform. An Arduino controller was programmed to control the position of Mover 3 based on the ultrasonic sensor range value. If optimally implemented, Mover 3 will cancel the undesirable Mover 2 motion. The test platform hardware configuration is shown in Fig. 4.

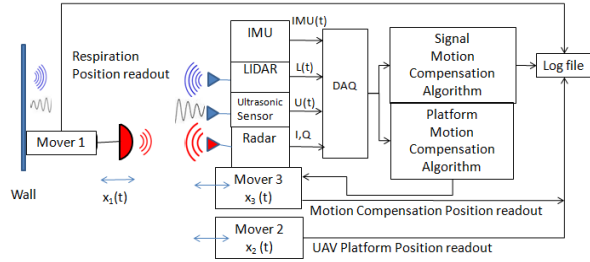


Fig. 3. Motion compensation experiment configuration block diagram. The respiration signal of interest (Mover 1) is detected by the radar that is mounted on the motion compensator (Mover 3) that is mounted on the base platform representing the unwanted motion from a UAV (Mover 2).

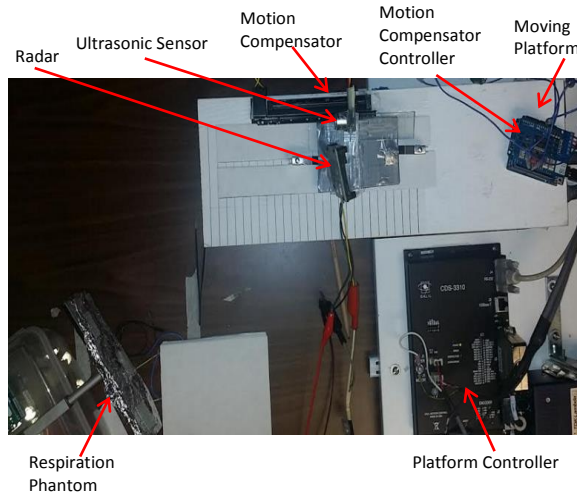


Fig. 4. Top view of motion compensation test bench components. Motion compensator (top center) is mounted on white plate mounted on platform motion actuator. Ultrasonic sensor is pointed at flat plate to the left (not shown) representing the ground. Radar is pointed at respiration phantom (lower left).

D. Ultrasonic sensor for feedback motion compensation

We focused on the ultrasonic sensor for this paper. Ultrasonic sensors operate by emitting high frequency pulses that are then reflected by a target. After reflecting off the target, the echo is then received by the sensor and the time difference is measured. With the time difference, the distance of the object can be calculated using the speed of sound. The IMU and lidar sensors will be tested in the future when the sensor fusion algorithm is developed and refined.

E. Motion compensation algorithm

A motion controller from Galil and mover were operated using code designed in Galil Tools. The controller made the mover perform a sinusoidal motion emulating the undesired platform motion. Additional

code was written for an Arduino Uno controller that controlled the motion compensation mover. The Arduino code reads the output from the ultrasonic sensor and moves the motion compensation actuator relative to the difference between the received distance value and a reference distance value.

A PID (Proportional, Integral, Derivative) stage was also implemented in the feedback algorithm as shown in Fig. 5. The PID parameters allows for tuning of the feedback response to optimize the motion compensation. The optimal PID values were empirically derived as $P = 68$, $I = 7.6$ and $D = 73$. We also modeled the system transfer function using the Matlab System ID Toolbox to reduce the number of PID empirical permutations.

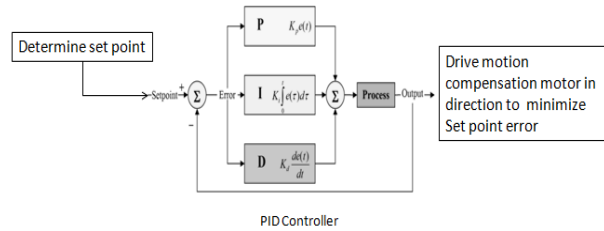


Fig. 5. PID controller in the motion compensation feedback loop.

IV. EXPERIMENT RESULTS

With the motion compensation enabled, the platform motion was reduced from 4.6 cm to 1.1 cm peak-to-peak for a 76% reduction in unwanted motion as shown in Fig. 6. This result was based on a constant gain feedback signal. After tuning the PID loop, we were able to reduce the compensated peak-to-peak motion to 0.6 cm for an 86% reduction in unwanted motion.

We also attempted to improve the compensation response with a position dependent gain factor, where the gain was proportional to the error voltage, resulting in faster convergence of the motion compensation. The result was not as significant as the PID result and was abandoned.

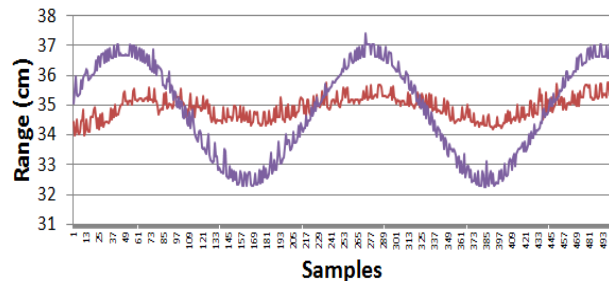


Fig. 6. Platform motion with 4.6 cm peak-to-peak sinusoidal waveform and 1.1 cm peak-to-peak compensated motion for a 76% reduction in unwanted platform motion amplitude using the constant gain feedback loop.

To assess the motion compensation system performance, we plotted the spectrum of the respiration signal alone (Fig. 7 (a)), the platform motion spectrum (Fig. 7 (b)), and the compensated simultaneous respiration and platform motion spectrum (Fig. 7 (c)). The spectra were obtained by performing a FFT in MatLab from the baseband radar signal. As shown in Fig. 7 (b), the respiration signal is masked by the platform motion noise. In Fig. 7 (c), the respiration signal is recovered after motion compensation is enabled.

The SNR for each case shown in Fig. 7 is summarized in Table 1.

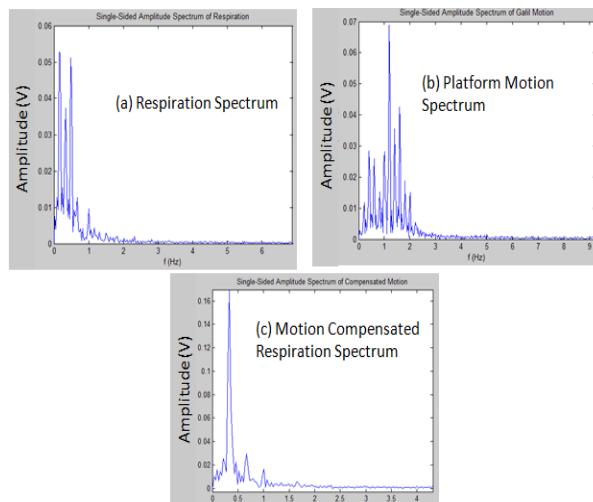


Fig. 7. Baseband radar spectra for: (a) respiration signal at 0.4 Hz, (b) platform motion at 1.1 Hz, and (c) both respiration and platform motion with motion compensation enabled.

Table 1: SNR with and without motion compensation

	Voltage (V)		Power (V^2)		SNR (dB)
	Respiration	Motion	Respiration	Motion	
No compensation	0.028	0.07	0.0008	0.0049	-8.0
Motion compensation	0.17	0.015	0.0289	0.0002	21.1
SNR improvement					29.1

V. CONCLUSION

We demonstrated that unwanted platform motion can be compensated for, thereby improving the SNR of a Doppler radar signal. Analysis and simulation of secondary sensors to derive motion compensation signals in a feedback control system and empirical measurements with an ultrasonic sensor were conducted to compensate for unwanted platform motion. The experimental result was a 29 dB improvement in SNR. Future work will investigate other sensor types and

multiple sensors with sensor fusion to further increase the system performance.

ACKNOWLEDGEMENTS

This work was supported in part by Award No. U54MD007584 from the National Institute on Minority Health and Health Disparities (NIMHD), National Institutes of Health (NIH), National Science Foundation (NSF) under grants CBET-1160326, ECS-0702234, ECCS-0926076, the University of Hawaii at Manoa REIS, and by Department of Energy grant DEOE0000394.

REFERENCES

- [1] V. Ferrara, "Technical survey about available technologies for detecting buried people under rubble or avalanches," *WIT Transactions on The Built Environment*, vol. 150, pp. 91-101, May 2015.
- [2] L. Ren and A. E. Fathy, "Noncontact heartbeat detection using UWB impulse Doppler radar," in *IEEE Radio Science Meeting*, Vancouver, BC, Canada, pp. 221, July 2015.
- [3] C. Li and J. Lin, "Random body movement cancellation in Doppler radar vital sign detection," *IEEE Trans. on Microw. Theory Techn.*, vol. 56, no. 12, pp. 3143-3152, Nov. 2008.
- [4] R. Sabatini, C. Bartel, A. Kaharkar, and T. Shaid, "Design and integration of vision based sensors for unmanned aerial vehicles navigation and guidance," *Proceedings of the SPIE, Optical Sensing and Detection II*, vol. 8439, Apr. 16-19, 2012.
- [5] L. Xinhua and Y. Cao, "Research on the application of the vision-based autonomous navigation to the landing of the UAV," *Proceedings of 5th International Symposium on Instrumentation and Control Technology*, vol. 5253, pp. 385-388, Oct. 24-27, 2003.

Radar Noise Floor Method for Occupancy Detection

Pooja Nuti¹, Ehsan Yavari², and Olga Boric-Lubecke¹

¹ Department of Electrical Engineering
University of Hawaii at Manoa, Honolulu, HI 96822, USA
poojan@hawaii.edu, olgabl@hawaii.edu

² Adnoviv LLC
Adnoviv LLC, Honolulu, HI 96822, USA
ehsan@adnoviv.edu

Abstract — A 2.4 GHz continuous wave Doppler radar sensor is utilized to carry out occupancy detection through detection of human presence over an empty room based on time domain root-mean-square (RMS) values. An existing system-on-chip with custom-made baseband board is employed for developing the radio.

Index Terms — Doppler radar, noise level, occupancy detection, Root-Mean-Square (RMS).

I. INTRODUCTION

Previously, occupancy detection has been conducted through detection of large motions or heat detection. Occupancy sensing technology is now moving away from such methods towards vital sign detection. In an effort to design such an occupancy sensor, noise level in conjunction with root-mean-square (RMS) is utilized [4].

Additionally, by rapid increase in global energy use, majority coming from fossil fuels, energy efficiency and conservation are becoming increasingly important. Studies show occupancy sensors can save up to 50% of that energy use [1]. Passive infrared and ultrasonic sensors are the two most common occupancy sensors in the market, however, they suffer from high rates of false alarms due to inconsistent ability to distinguish occupancy [2]. The feasibility of Doppler radar as an occupancy sensor is investigated in [3]. In [4] we investigated the effects of motion on the noise floor of a room and the potential to use that as a measure to discern an occupied room vs. an unoccupied one. In this paper we present experimental results with a human occupant, confirming that this technique can be used to discern human presence.

II. EXPERIMENTAL SETUP

A custom radar with single antenna is used for the measurements (Fig. 1). Radar transmits 2.4 GHz signal.

The radiated signal will be reflected back and received by same antenna. The received signal after down conversion and a conditioning circuit is digitized by the onboard ADC. The digitized signal is sent to a computer via usb port.

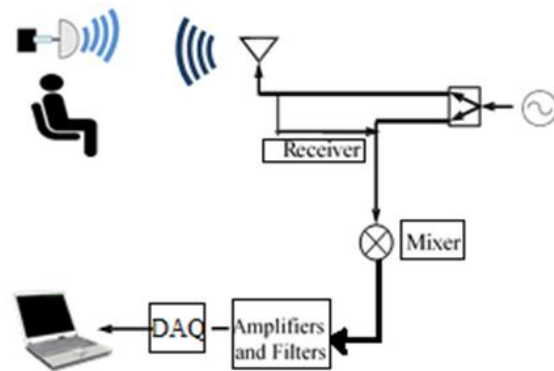


Fig. 1. Block diagram of system.

National Electrical Manufacturers Association (NEMA) standards are adhered to in order to obtain valid data during collection. NEMA requires that occupancy sensors be tested in an indoor area. The indoor area should be split into uniform cells in a grid pattern. By standards, these cells should be 3ft by 3ft in area. The testing environment should be controlled, such that temperature and humidity remain constant. In order to meet these requirements, a room with dimensions 3.5 m by 4.5 m with no windows was utilized. Additionally, the room was broken into 27 cells where the mechanical target/human subject used for vital-sign modeling could be moved through. See Fig. 2 for cell layout in room. Blue tapes in Fig. 3 mark the mechanical target locations throughout the room. The occupancy sensor along with passive infrared/ultrasonic hybrid sensor were wall-mounted. As per standard, the direction of motion

Ehsan Yavari² was with University of Hawaii at Manoa, Honolulu HI 96822, USA. He is now VP of Research at Adnoviv LLC, Honolulu HI 96822, USA

produced by the mechanical target was perpendicular to the sensor face.

Radar is used to detect presence in the room by detecting small periodic motions such as respiration in each individual cell. A precision single-axis linear stage is from Galil motion control (CDS-3310) with a pulse-width modulation (PWM) driver is employed for generating such periodic motions simulating human respiration. This mechanical target was moved throughout 27 full cells and radar return from the target at each of the 27 cells was recorded. The duration of recordings in each of the 27 cells was 90 seconds. A similar test with a human subject in place of the mechanical target was also performed under same conditions. Additionally, data collections were taken consisting of radar reflected signal from the same empty room with no mechanical target for estimating noise level in our measurements.

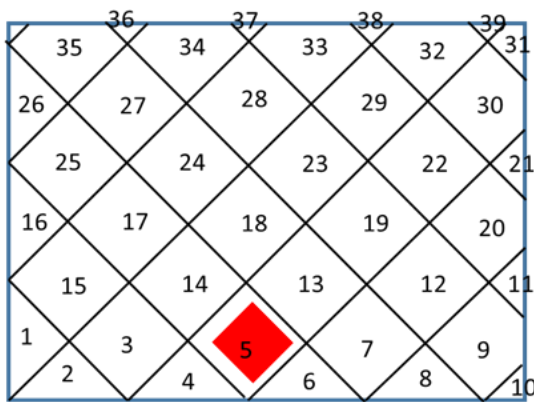


Fig. 2. Room layout consisting of 27 cells used for data collection. Note Cell 5 location in front of sensor face.



Fig. 3. Test setup [4].

III. EXPERIMENTAL RESULTS

Analysis of data included plotting time-domain profiles to qualitatively observe the radar return from different cells, and noise return. Additionally, RMS was

applied to all data collects to further quantify signal level for comparison purposes.

A. Results of tests with mechanical target

In the time domain, radar data from tests using a mechanical target can look similar to data collected from the radar with an empty room. This results in difficulty distinguishing between noise and radar signals. The similarities between radar signal from a mechanical target and noise are observed in comparing amplitudes of Figs. 4 and 5 to that of Fig. 6. These figures depict the reflected signal from a mechanical target at different locations in the testing room. After studying the raw radar data from each of the 27 cells tested, we found Cell 5 to have the strongest signal due to the closeness (0.5m) and perpendicularity to the radar antenna. Cell 21 is farther away from the radar field of view and has the weakest signal. The RMS value of Cell 5 is .2432 units and the RMS value of Cell 21 is .2538 units, comparatively the RMS of one set of empty room data (noise) is 0.2439 units. These values illustrate the similarities in return.

In order to account for the amplitude fluctuations observed in the signal the root mean square (RMS) of the time-domain data from various cells were taken. RMS is also used because it can account for both non-periodic variability associated with signal return from radar and noise, and also be compared easily. The built-in RMS function provided in Matlab was used to take the RMS of data matrices. The used RMS in these tests are defined in [4]. RMS was taken of the time domain data of radar from mechanical target in all 27 cells/locations in the room and compared with the RMS values of multiple noise recordings. The result of plotting both noise and radar data from mechanical target is shown in Fig. 6.

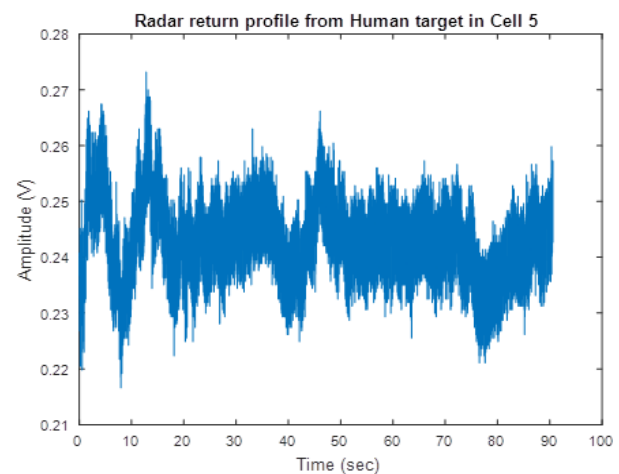


Fig. 4. Radar data from mechanical target in region of strong radar return.

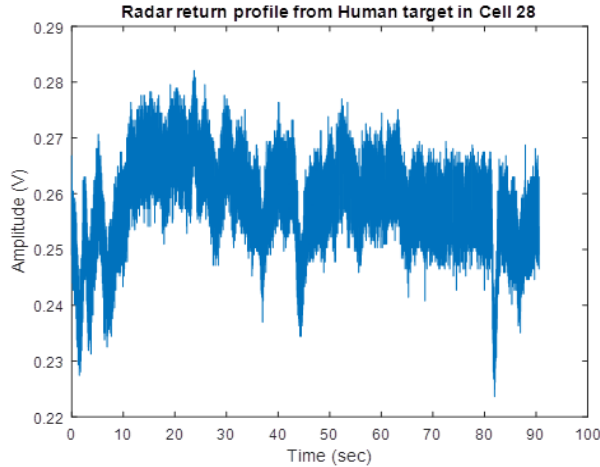


Fig. 5. Radar data from mechanical target in region of weak radar return.

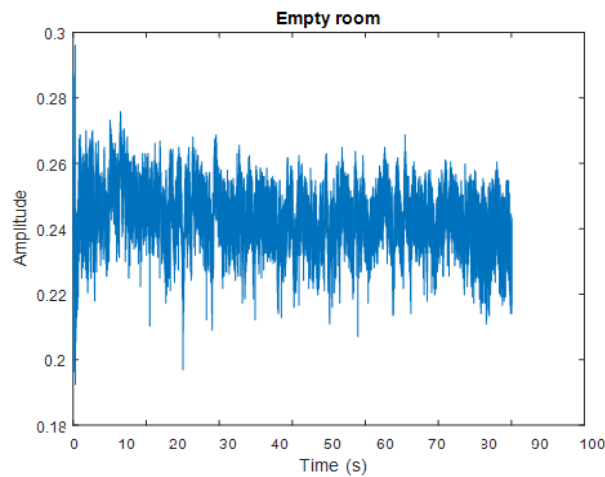


Fig. 6. Radar signal from empty room no mechanical target.

Figure 7 illustrates that despite the raw noise data and radar data with mechanical target seeming qualitatively similar; there is a distinction between their time domain RMS values. The mean of the RMS values of mechanical target return is 0.2523 units while the mean of RMS values of noise (empty room return) is 0.2430 units. These values yield an average difference of 0.0093 units. This difference is low due to the low frequency utilized in data collection (0.2 Hz). Radar baseband filters may have contributed to the low difference between radar signals with the mechanical target and noise data. The difference between mechanical target return and noise is consistent. 92.6% radar signal from the mechanical target could be distinguished from noise, as two RMS values

(corresponding to data collects from two unique cells) from mechanical target are within noise region and therefore undistinguishable.

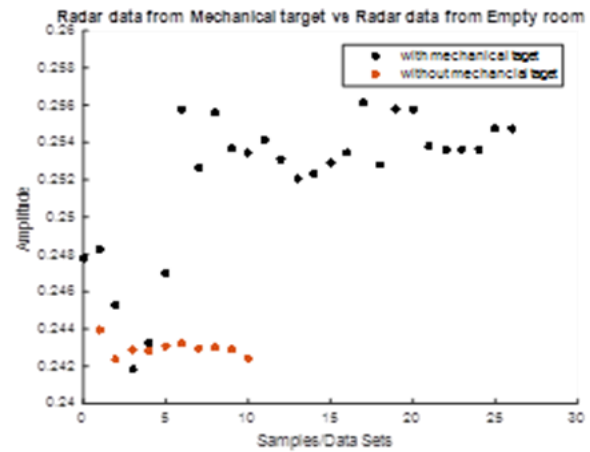


Fig. 7. Time domain RMS with and without mechanical target [4].

B. Results of tests with human subject

There is a qualitative difference between RMS amplitudes of return from a mechanical target in Fig. 7 and a human target (Fig. 10). Using a mechanical target resulted in a more distinct signal level from motion due to the more similar and concentrated amplitudes. In Fig. 10, the RMS amplitudes from the human target are less concentrated than that of the mechanical target. This may be due to the less-controlled frequency of periodic motion observed in human respiration in comparison to the constant frequency that the mechanical target operates at. The result of radar return from human respiration matches the result of radar return from a mechanical target. In these tests, a human was placed in each of the same 27 cells used to test the mechanical target. Similar to the results of the mechanical target, strongest return from the target was yielded from Cell 5 which is located right in front of radar antenna (see Fig. 8). The RMS amplitude of return from this cell was .2495 V. The ability of radar to detect vital signs is observed through the sinusoidal waveform (Fig. 8). This sinusoidal motion corresponds to human respiration. As the human target is moved into cells farther from the line of sight of antenna, radar return degrades. In Fig. 9, Cell 22 yields the lowest RMS amplitude of radar return (.2436 V). This lower amplitude is due to the distance between the radar antenna and test subject, and the location of cell 22 is not in direct path of antenna but rather on a side of the room. Despite the lower amplitude, the presence of a human target is still detected over the mean noise level of .2430 V.

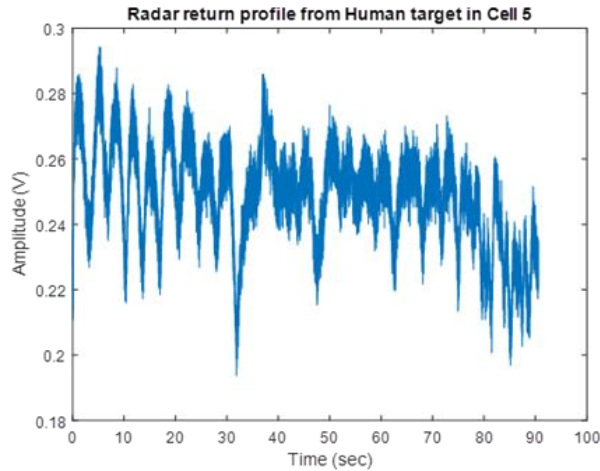


Fig. 8. Human respiration observed through sinusoidal waveform in time-domain.

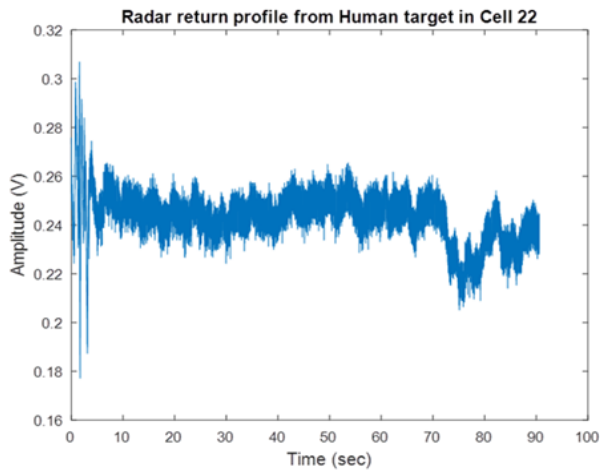


Fig. 9. Radar return from human target at distance away from antenna line of sight. Note similar profile to noise.

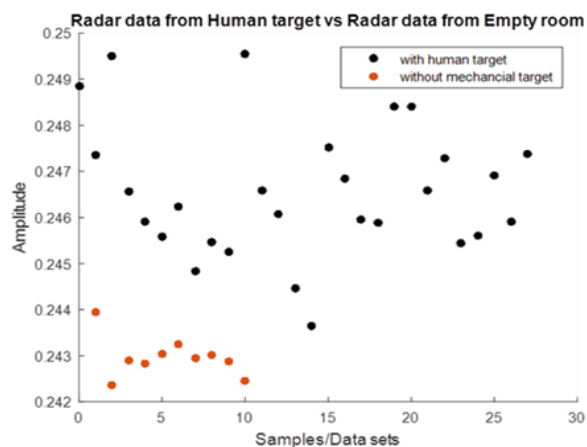


Fig. 10. Return from human target at generally higher signal level than noise level.

IV. CONCLUSION

A Doppler radar occupancy sensor was used for detecting presence. Noise floor of a room is used as a measure to detect occupancy. Experiments were performed to distinguish empty room radar return versus radar return from a mechanical target simulating respiration signal and human target with a resting respiration rate. Tests with a mechanical target agree with tests with a human target. In both cases, stronger human presence is observed in cells closest to the radar. Additionally, both cases result in 93% accuracy in detection of human presence over noise. The gap between RMS values can be utilized to distinguish movement from noise. Future work would focus on testing radar at different frequencies and quantifying the noise floor for the system. Additionally, future work could include modeling performance of radar and finding limits to which this method of occupancy detection is valid by attempting human presence detection over different environments.

ACKNOWLEDGMENT

This work was supported in part by National Science Foundation (NSF) under grant STTR-1417308.

REFERENCES

- [1] X. Guo, D. K. Tiller, G. P. Henze, and C. E. Waters, "The performance of occupancy-based lighting control systems: A review," *Lighting Research and Technology*, vol. 42, no. 4, pp. 415-431, 2010.
- [2] M. Kumar, D. Garge, and R. Zachery, "Multi-sensor fusion strategy to obtain 3-D occupancy profile," *Proceedings of the 31st Annual Conference of the IEEE Industrial Electronics Society (IECON)*, pp. 2083-2088, 2005.
- [3] E. Yavari, H. Jou, V. Lubecke, and O. Boric-Lubecke, "Doppler radar sensor for occupancy monitoring," in *Proc. 2013 IEEE Radio Wireless Symp.*, pp. 316-318, 2013.
- [4] E. Yavari, P. Nuti, and O. Boric-Lubecke, "Occupancy detection using radar noise floor," in *Proc. ICWITS/ACES 2016 Conference*, pp. 152-154, 2016.

UAV-Radar System for Vital Sign Monitoring

Ashikur Rahman, Yuta Ishii, and Victor Lubecke

Department of Electrical Engineering
University of Hawaii at Manoa
Honolulu, USA

Abstract — Feasibility and fabrication of components of a life-sign radar system on unmanned aerial vehicle (UAV) has been studied. A signal conditioning circuit has been simulated, fabricated, and tested for data preparation and acquisition. Application such as, vital-sign detection, using UAV in real-time requires wireless transmission of baseband data to the monitoring station. Methods have been devised to achieve this goal. A quadrature Doppler radar has been assembled using two single channel x-band MDU1020 radars. The united radars can avoid null point distortion in physiological monitoring. Examinations were performed with both mechanical targets.

Index Terms — Amplifier, demodulation, Doppler radar, filter, microwave, phase, phase noise.

I. INTRODUCTION

Short distance Doppler radars have been thoroughly studied and reported in RF based noninvasive measurements. Short distance radars can detect small motions (mm or submillimeter, based on frequency of operation) and hence can be used in vital sign measurements based on respiratory effort. In vital sign measurements continuous wave (CW) Doppler radar uses RF echo reflected from human torso. The phase of echo is proportional to the variable displacement across the body surface corresponding to the motion of heart and lungs. Due to the high sensitivity of short distance radar any motion artifact will distort the received RF signal bounced off any moving surface. Some potential application of vital sign measurements from a mobile platform can be very useful. For example, a UAV carrying a vital sign radar can be used as first responder in a battle field or a search and rescue robot during natural catastrophe. Such a system requires a portable vital-sign radar system, a data acquisition and processing system as shown in Fig. 1.

Single channel vital sign radar has major limitation since a null case may arise in numerous positions in front of the radar which gives inaccurate measurement [1]; hence, quadrature radar is preferred. Some manufacturers produce cheap single channel motion detector radars for specific purposes, i.e., MDU1020 motion detector by

Microsemi. These radars are application specific and subject to null point distortions depending on the nominal distance of the target and the radar. However, two of these radars can be placed in a way to avoid the single channel radar's constraint providing a cost effective means of vital sign detection [2]. Commercial motion detection units (MDU) or vital sign radars have reasonably good power output; 13-dBm, for instance, in a MDU 2400 module mass-produced by Microwave Solutions Ltd.

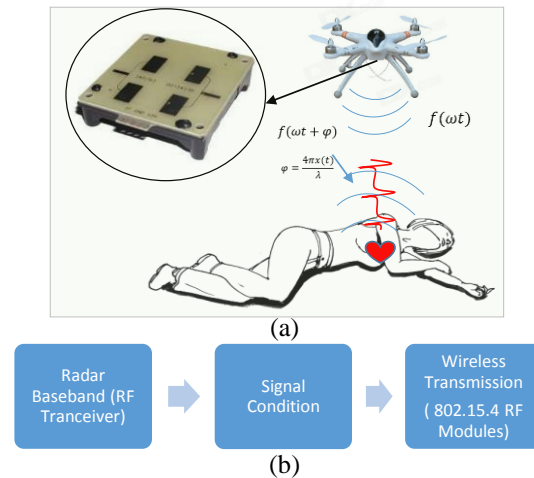


Fig. 1. An illustration of life sign detection using short distance radars reveals: (a) UAV mounted radar (MDU-1020) for vital sign detection, and (b) shows a block diagram of the system components [3].

However, the baseband signal output is only a small portion of 13-dBm, due to the fact that vital sign related motion is very small compared to the radar's full range of exposure ability. This imposes the fact that the radar signal needs to be enhanced prior to sending the output to a communication link. A feasible solution is to apply ZigBee based on the IEEE 802.15.4 protocol. ZigBee device's analog sampling is limited to the range of 0 to 1.2 volts. Testing several MDU's over a range of a meter, the MDU's voltage output swing was found to be -20 mV to 20 mV for respiration which may easily be buried in

the noise during wireless transmission [3]. Moreover, since the ZigBee device cannot sample negative voltages, the radar output needs to be shifted, amplified and filtered. Integrating these functions requires a custom design of signal conditioning circuitry.

II. SYSTEM ARCHITECTURE

Radar measurement from a mobile platform is modulated by the motion artifact introduced by the mobile platform. The combined motion may show phase distortion, and saturation problems in received backscattered signal. Additionally, the occurrence of null points in the received radar signal makes the extraction of life signs challenging [4], [5]. These issues stem from inconstant traveling distance seen by backscattered RF between the radar antenna and the target [5]. A motion compensation technique for mobile CW Doppler vital signs radar has been demonstrated using high precision cameras [5]. Another work included development of a new, field applicable, low-cost methodology for motion artifact compensation using only a small RF tag [5]. Some other techniques related to vital sign measurements were reported in [6]-[8]. However, these works either focused on body motion cancellation, whereas, our work focuses on vital sign detection from a UAV. Additional sensors can characterize UAV platform motion to filter out the noise introduced by vibration and drift. The output of these sensors also requires some conditioning (amplification and filtering) as shown in the detailed system architecture in Fig. 2.

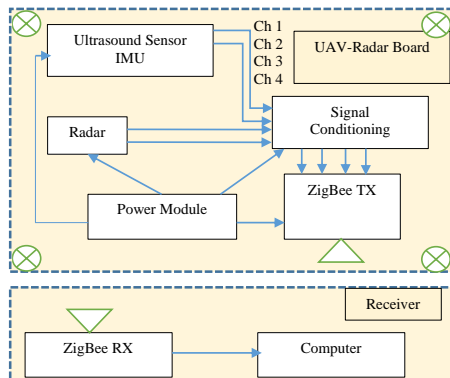


Fig. 2. A detail system diagram of UAV radar system for vital sign monitoring.

Application of ultrasound sensor can generate and approximate spatial map (in a confined space, or ground elevation for open space) of a moving object within the range of speed and sensitivity. This can help characterize platform motion, hence, useful data for radar signal processing in noise cancellation.

To test the concept by starting from the scratch, we needed low cost radars, able to perform demodulation of

signal with greater quality. On the other hand, recorded signal needs to be cleaned up for further processing and filtering unwanted components. So, this worked focused on finding an engineering solution to a low cost radar also creation of custom signal conditioning circuit.

III. LOW COST RADAR SENSOR

We proposed a low cost solution to an IQ radar system. The price is well under of existing solutions. A typical quadrature radar MDU-4200 from Microwave Solution Ltd. Costs about \$120, whereas, a single-channel MDU 1020 can be found as low as \$7. A theoretical explanation presented below justifies the composition of two single channel radars for making an alternate solution to quadrature radar.

A. Radar theory of vital sign detection

A typical coherent continuous wave vital sign Doppler radar system sends an RF signal towards human torso, the echo is phase modulated due to the positional variation of moving body parts. The echo is mixed and down converted to retrieve the target's displacement. The output of a single channel receiver is given by [1]:

$$B(t) \approx A_B \cos \left(\theta + \frac{4\pi x(t)}{\lambda} + \frac{4\pi y(t)}{\lambda} + \Delta\phi \left(t - \frac{2d_0}{c} \right) \right), \quad (1)$$

where θ is constant phase shift and $\Delta\phi$ is residual phase noise. A_B , λ , $x(t)$, $y(t)$, and d_0 are baseband amplitude, wavelength, chest movement, heart movement and nominal distance between the radar and the target. Now, if somehow $\frac{\pi}{2}$ phase change is introduced, (1) will result in:

$$B(t) \approx A_B \sin \left(\theta + \frac{4\pi x(t)}{\lambda} + \frac{4\pi y(t)}{\lambda} + \Delta\phi \left(t - \frac{2d_0}{c} \right) \right). \quad (2)$$

Our work proves that physical offset between two single-channel radars can achieve proper phase shift for quadrature radar channels.

B. Null and optimum demodulation

The constant phase shift in (1) is related to nominal distance and can be expressed as:

$$\theta = \frac{4\pi d_0}{\lambda} + \theta_0; \quad d_0 = \frac{\lambda(\theta - \theta_0)}{4\pi}; \quad d_0 = \frac{\lambda \left(\frac{k\pi}{2} - \theta_0 \right)}{4\pi}. \quad (3)$$

If θ is denoted as the k multiple of $\frac{\pi}{2}$, the baseband output $B(t)$ will be either null or optimum for an integer value of k when small signal approximation is applicable [1]. From (1) and (2) we see that null and optimum baseband output occurs for the nominal distances as:

$$d_{NULL} = \frac{\lambda(m\pi - \theta_0)}{4\pi}; \quad d_{OPT} = \frac{\lambda \left(m\pi + \frac{\pi}{2} - \theta_0 \right)}{4\pi}, \quad (4)$$

where m is an integer. (3) reveals that the adjacent null and optimum separation is:

$$|d_{NULL} - d_{OPT}| = \frac{\lambda}{8}. \quad (5)$$

This examination proves the fact that if two single channel radars are oriented in similar way with a separation of $\frac{\lambda}{8}$ in the plane of nominal distance between

the target and the radar transceivers, one of the radars will be in optimum position given that the other is in null position and vice versa [2]. One fundamental assumption is that the difference of the residual phase noise of the radars is negligible.

C. Fabrication and testing

Two MDU1020 radars were used for the experiment. MDU1020 has the operating frequency is 10.525 GHz. The theoretical distance between consecutive null and optimum points is $3.5629 \text{ mm}; \frac{\lambda}{8}$ in other words [2]. Now creating the physical separation of this length in traveling plane of the wave should ensure fail-safe design. In case the nominal distance between one of the radars is in null position, the other will be in optimum position. The two radars were physically separated approximately 3.5 mm, as shown in Fig. 3. A mechanical mover was programmed to move in 0.5 Hz sinusoidal motion. The nominal distance between the radar pair and target was varied in the range of [0.5 m (0.5+.0035) m]. Linear demodulation has been performed using the output (voltage proportional to displacement) of the two radars as shown in Fig. 4.

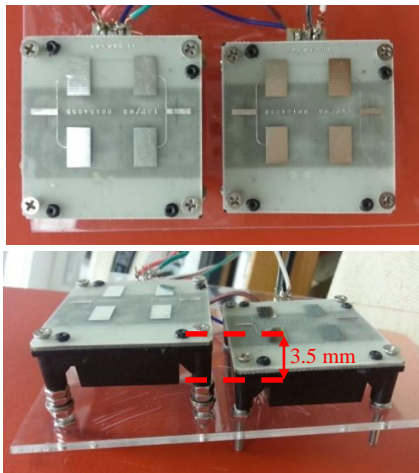


Fig. 3. Quadrature radar assembly is illustrated. A physical offset of approximately 3.5 mm has been kept between the two MDU1020 single channel k band radars [2].

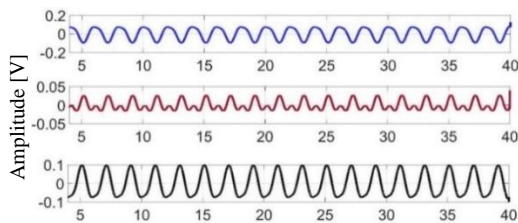


Fig. 4. Shows the two radar output and combined output when the nominal distance is gradually changed. It is evident that one radar suffers distortion, but the other radar helps demodulating the correct signal [2].

IV. SIGNAL PROCESSING MODULE

A. Design requirement

The design requirements of the signal conditioning circuit are amplification, filtering, light-weight, DC offsetting capability for level shifting.

B. Simulation

General purpose uA741 operational amplifiers were selected for design and fabrication of the quick prototype. The circuit has two stages as shown in Fig. 5. The first stage is a voltage follower while the second stage is a summing inverting amplifier. Passive components have been used for filtering, i.e., variable resistors along with capacitors were used to provide DC offset, tunable band and gain. Figure 6 shows some tuning simulation.

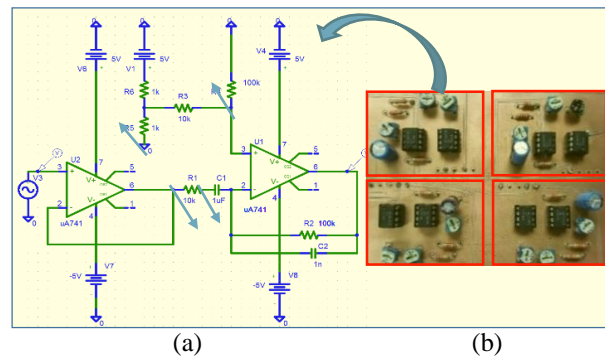


Fig. 5. Software simulation and layout is shown: (a) depicts the circuit diagram of the single channel amplifier, and in (b) fabricated circuit containing four amplifier blocks [3].

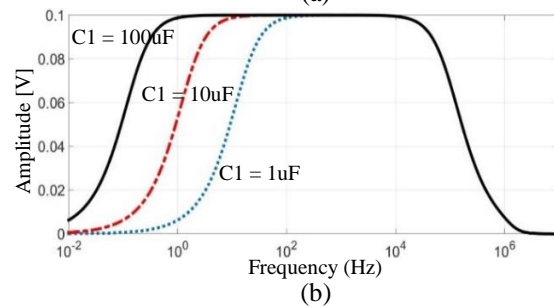
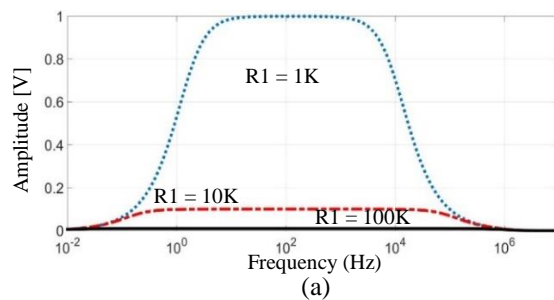


Fig. 6. Bandwidth and gain variation by tuning resistance in (a), and capacitance in (b). R1 and C1 in Fig. 5 (a) were varied.

C. Fabrication and testing

PCB layout was made using a LPKF mid-range PCB milling machine. A double sided FR-4 board was used to print the layout. A four-channel signal conditioning circuit was designed, so the circuit is capable of conditioning four channels.

V. RESULTS

Experiments were to check the performance of signal conditioning, wireless data acquisition. Target's motion and a simple platform motions were simulated using mechanical moving stages, as demonstrated in Fig. 7. The radar sensor and signal conditioning circuitry was mounted on a linear stages. Figure 8 illustrates the presence of noise in radar signal due to motion artifact simulated using linear stage. The radar sensor data was recorded via ZigBee communication link.

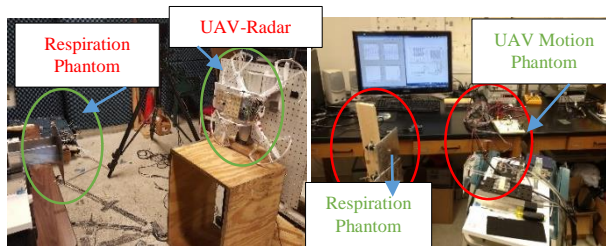


Fig. 7. (a) Shows experimental assembly, a DJI phantom quadcopter carrying the circuitry, and (b) shows experiments, simulating platform motion and target motion with two different linear stage.

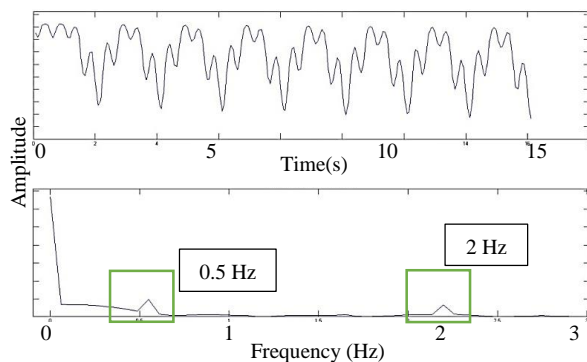


Fig. 8. Shows the time and frequency domain plots of radar data that contains two motion signature, platform motion was 2 Hz and target motion was 0.5 Hz simple periodic motion. Both platform motion and target's motion are in composite signal.

VI. CEM APPLICATION

This work implemented off-the-shelf radar having vertical and horizontal polarization of 36 degree, and 72 degree respectively in patch antenna. For motion artifact compensation low-IF RF tags can be used. A

computational EM (CEM) simulation will help making a robust system.

VII. CONCLUSION

UAV-Life sign Radar system has been studied and system components were built to provide a low cost fabrication of the platform. A low noise lightweight four-channel amplifier with DC offsetting and frequency tuning capability was fabricated. A low cost solution for quick prototyping of distortion-less radars system has been proposed with practical implementation. Overall, our work opens up the potentials for using UAV for life sign monitoring.

REFERENCES

- [1] A. Droitcour, V. Lubecke, J. Lin, and O. Boric-Lubecke, "A microwave radio for Doppler radar sensing of vital signs," in *IEEE MTT-S Int. Microw. Symp. Dig.*, Phoenix, pp. 175-178, 2001.
- [2] A. Rahman, E. Yavari, and V. Lubecke, "Single channel radar fusion for quadrature life-sign Doppler radar," in *IEEE ACES*, Honolulu, pp. 1-2, 2016.
- [3] A. Rahman, A. Nakahara, R. Nakata, and V. Lubecke, "Signal conditioning for UAV-radar in vital sign monitoring," in *IEEE ACES*, Honolulu, pp. 1-2, 2016.
- [4] A. Rahman, E. Yavari, X. Gao, V. Lubecke, and O. Boric-Lubecke, "Signal processing techniques for vital sign monitoring using mobile short range Doppler radar," in *IEEE Radio Wireless Symp.*, San Diego, CA, pp. 1-3, 2015.
- [5] A. Rahman, E. Yavari, V. Lubecke, and O.-B. Lubecke, "A low-IF tag-based motion compensation technique for mobile doppler radar life sign monitoring," *IEEE Transactions on Microwave Theory and Techniques*, vol. 63, no. 10, pp. 3034-3041, Oct. 2015.
- [6] L. Ren and A. E. Fathy, "Noncontact heartbeat detection using UWB impulse Doppler radar," in *IEEE Radio Science Meeting*, Vancouver, BC, Canada, pp. 221, July 2015.
- [7] V. Ferrara, "Technical survey about available technologies for detecting buried people under rubble or avalanches," *WIT Transactions on the Built Environment*, vol. 150, pp. 91-101, May 2015.
- [8] C. Li and J. Lin, "Random body movement cancellation in Doppler radar vital sign detection," *IEEE Trans. on Microw. Theory Techn.*, vol. 56, no. 12, pp. 3143-3152, Nov. 2008.

INFORMATION FOR AUTHORS

PUBLICATION CRITERIA

Each paper is required to manifest some relation to applied computational electromagnetics. **Papers may address general issues in applied computational electromagnetics, or they may focus on specific applications, techniques, codes, or computational issues.** While the following list is not exhaustive, each paper will generally relate to at least one of these areas:

1. **Code validation.** This is done using internal checks or experimental, analytical or other computational data. Measured data of potential utility to code validation efforts will also be considered for publication.
2. **Code performance analysis.** This usually involves identification of numerical accuracy or other limitations, solution convergence, numerical and physical modeling error, and parameter tradeoffs. However, it is also permissible to address issues such as ease-of-use, set-up time, run time, special outputs, or other special features.
3. **Computational studies of basic physics.** This involves using a code, algorithm, or computational technique to simulate reality in such a way that better, or new physical insight or understanding, is achieved.
4. **New computational techniques** or new applications for existing computational techniques or codes.
5. **“Tricks of the trade”** in selecting and applying codes and techniques.
6. **New codes, algorithms, code enhancement, and code fixes.** This category is self-explanatory, but includes significant changes to existing codes, such as applicability extensions, algorithm optimization, problem correction, limitation removal, or other performance improvement. **Note: Code (or algorithm) capability descriptions are not acceptable, unless they contain sufficient technical material to justify consideration.**
7. **Code input/output issues.** This normally involves innovations in input (such as input geometry standardization, automatic mesh generation, or computer-aided design) or in output (whether it be tabular, graphical, statistical, Fourier-transformed, or otherwise signal-processed). Material dealing with input/output database management, output interpretation, or other input/output issues will also be considered for publication.
8. **Computer hardware issues.** This is the category for analysis of hardware capabilities and limitations of various types of electromagnetics computational requirements. Vector and parallel computational techniques and implementation are of particular interest.

Applications of interest include, but are not limited to, antennas (and their electromagnetic environments), networks, static fields, radar cross section, inverse scattering, shielding, radiation hazards, biological effects, biomedical applications, electromagnetic pulse (EMP), electromagnetic interference (EMI), electromagnetic compatibility (EMC), power transmission, charge transport, dielectric, magnetic and nonlinear materials, microwave components, MEMS, RFID, and MMIC technologies, remote sensing and geometrical and physical optics, radar and communications systems, sensors, fiber optics, plasmas, particle accelerators, generators and motors, electromagnetic wave propagation, non-destructive evaluation, eddy currents, and inverse scattering.

Techniques of interest include but not limited to frequency-domain and time-domain techniques, integral equation and differential equation techniques, diffraction theories, physical and geometrical optics, method of moments, finite differences and finite element techniques, transmission line method, modal expansions, perturbation methods, and hybrid methods.

Where possible and appropriate, authors are required to provide statements of quantitative accuracy for measured and/or computed data. This issue is discussed in “Accuracy & Publication: Requiring, quantitative accuracy statements to accompany data,” by E. K. Miller, ACES Newsletter, Vol. 9, No. 3, pp. 23-29, 1994, ISBN 1056-9170.

SUBMITTAL PROCEDURE

All submissions should be uploaded to ACES server through ACES web site (<http://aces-society.org>) by using the upload button, Express Journal section. Only pdf files are accepted for submission. The file size should not be larger than 6MB, otherwise permission from the Editor-in-Chief should be obtained first. Automated acknowledgment of the electronic submission, after the upload process is successfully completed, will be sent to the corresponding author only. It is the responsibility of the corresponding author to keep the remaining authors, if applicable, informed. Email submission is not accepted and will not be processed.

EDITORIAL REVIEW

In order to ensure an appropriate level of quality control, papers are peer reviewed. They are reviewed both for technical correctness and for adherence to the listed guidelines regarding information content and format.

PAPER FORMAT

Only camera-ready electronic files are accepted for publication. The term **“camera-ready”** means that the material is neat, legible, reproducible, and in accordance with the final version format listed below.

The following requirements are in effect for the final version of an ACES Express Journal paper:

1. The paper title should not be placed on a separate page. The title, author(s), abstract, and (space permitting) beginning of the paper itself should all be on the first page. The title, author(s), and author affiliations should be centered (center-justified) on the first page. The title should be of font size 14 and bolded, the author names should be of font size 12 and bolded, and the author affiliation should be of font size 10 (regular font, neither italic nor bolded).
2. An abstract is required. The abstract should be a brief summary of the work described in the paper. It should state the computer codes, computational techniques, and applications discussed in the paper (as applicable) and should otherwise be usable by technical abstracting and indexing services. The word "Abstract" has to be placed at the left margin of the paper, and should be bolded and italic. It also should be followed by a hyphen (–) with the main text of the abstract starting on the same line.
3. All section titles have to be centered and all the title letters should be written in caps. The section titles need to be numbered using roman numbering (I. II.)
4. Either British English or American English spellings may be used, provided that each word is spelled consistently throughout the paper.
5. Internal consistency of references format should be maintained. As a guideline for authors, we recommend that references be given using numerical numbering in the body of the paper (with numerical listing of all references at the end of the paper). The first letter of the authors' first name should be listed followed by a period, which in turn, followed by the authors' complete last name. Use a comma (,) to separate between the authors' names. Titles of papers or articles should be in quotation marks (" "), followed by the title of the journal, which should be in italic font. The journal volume (vol.), issue number (no.), page numbering (pp.), month and year of publication should come after the journal title in the sequence listed here.
6. Internal consistency shall also be maintained for other elements of style, such as equation numbering. Equation numbers should be placed in parentheses at the right column margin. All symbols in any equation have to be defined before the equation appears or right immediately following the equation.
7. The use of SI units is strongly encouraged. English units may be used as secondary units (in parentheses).
8. Figures and tables should be formatted appropriately (centered within the column, side-by-side, etc.) on the page such that the presented data appears close to and after it is being referenced in the text. When including figures and tables, all care should be taken so that they will appear appropriately when printed in black and white. For better visibility of paper on computer screen, it is good to make color figures with different line styles for figures with

multiple curves. Color should also be tested to insure their ability to be distinguished after black and white printing. Avoid the use of large symbols with curves in a figure. It is always better to use different line styles such as solid, dotted, dashed, etc.

9. A figure caption should be located directly beneath the corresponding figure, and should be fully justified.
10. The intent and meaning of all text should be clear. For authors who are not masters of the English language, the ACES Editorial Staff will provide assistance with grammar (subject to clarity of intent and meaning). However, this may delay the scheduled publication date.
11. Unused space should be minimized. Sections and subsections should not normally begin on a new page.

ACES reserves the right to edit any uploaded material, however, this is not generally done. It is the author(s) responsibility to provide acceptable camera-ready files in pdf and MSWord formats. Incompatible or incomplete files will not be processed for publication, and authors will be requested to re-upload a revised acceptable version.

COPYRIGHTS AND RELEASES

Each primary author must execute the online copyright form and obtain a release from his/her organization vesting the copyright with ACES. Both the author(s) and affiliated organization(s) are allowed to use the copyrighted material freely for their own private purposes.

Permission is granted to quote short passages and reproduce figures and tables from an ACES Express Journal issue provided the source is cited. Copies of ACES Express Journal articles may be made in accordance with usage permitted by Sections 107 or 108 of the U.S. Copyright Law. The consent does not extend to other kinds of copying, such as for general distribution, for advertising or promotional purposes, for creating new collective works, or for resale. The reproduction of multiple copies and the use of articles or extracts for commercial purposes require the consent of the author and specific permission from ACES. Institutional members are allowed to copy any ACES Express Journal issue for their internal distribution only.

PUBLICATION CHARGES

There is a \$200 basic publication charge assigned to each paper for ACES members, and \$300 charge for non-ACES members. Corresponding authors should be active members of the society at the time of submission and the time of publication in order to receive the reduced charge.

ACES Express Journal doesn't allow for more than four pages. All authors must comply with the page limitations. ACES Express Journal is an online journal, and printed copies are not available.

Upon completion of its first year, ACES Express Journal will be abstracted in INSPEC, in Engineering Index, DTIC, Science Citation Index Expanded, the Research Alert, and to Current Contents/Engineering, Computing & Technology.